frontiers in Earth Science

ORIGINAL RESEARCH
published: 17 December 2020
doi: 10.3389/feart.2020.594453

Brittle Deformation During Eclogitization of Early Paleozoic Blueschist

Michał Bukała[1,2], Christopher J. Barnes[1,3], Pauline Jeanneret[3,4], Károly Hidas[2,5], Stanisław Mazur[6], Bjarne S. G. Almqvist[3], Karolina Kośmińska[1], Iwona Klonowska[1,7], Juraj Šurka[8] and Jarosław Majka[1,3]*

[1]Faculty of Geology, Geophysics and Environmental Protection, AGH University of Science and Technology, Kraków, Poland, [2]Instituto Andaluz de Ciencias de la Tierra (IACT), CSIC and Universidad de Granada, Armilla, Spain, [3]Department of Earth Sciences, Uppsala University, Uppsala, Sweden, [4]Laboratoire Chrono-environnement, Université de Bourgogne-Franche-Comté, Besançon, France, [5]Departamento de Investigación y Prospectiva Geocientífica, Instituto Geológico y Minero de España, Tres Cantos, Spain, [6]Institute of Geological Sciences, Polish Academy of Sciences, Kraków, Poland, [7]Department of Earth and Environmental Sciences, Syracuse University, Syracuse, NY, United States, [8]Earth Science Institute, Slovak Academy of Sciences, Banská Bystrica, Slovakia

The Tsäkkok Lens of the Scandinavian Caledonides represents the outermost Baltican margin that was subducted in late Cambrian/Early Ordovician time during closure of the Iapetus Ocean. The lens predominantly consists of metasedimentary rocks hosting eclogite bodies that preserve brittle deformation on the μm-to-m scale. Here, we present a multidisciplinary approach that reveals fracturing related to dehydration and eclogitization of blueschists. Evidence for dehydration is provided by relic glaucophane and polyphase inclusions in garnet consisting of clinozoisite + quartz ± kyanite ± paragonite that are interpreted as lawsonite pseudomorphs. X-Ray chemical mapping of garnet shows a network of microchannels that propagate outward from polyphase inclusions. These microchannels are healed by garnet with elevated Mg relative to the surrounding garnet. Electron backscatter diffraction mapping revealed that Mg-rich microchannels are also delimited by low angle (<3°) boundaries. X-ray computed microtomography demonstrates that some garnet is transected by up to 300 μm wide microfractures that are sealed by omphacite ± quartz ± phengite. Locally, mesofractures sealed either by garnet- or omphacite-dominated veins transect through the eclogites. The interstices within the garnet veins are filled with omphacite + quartz + rutile + glaucophane ± phengite. In contrast, omphacite veins are predominantly composed of omphacite with minor apatite + quartz. Omphacite grains are elongated along [001] crystal axis and are preferably oriented orthogonal to the vein walls, indicating crystallization during fracture dilation. Conventional geothermobarometry using omphacite, phengite and garnet adjacent to fractures, provides pressure-temperature conditions of 2.47 ± 0.32 GPa and 620 ± 60°C for eclogites. The same method applied to a mesoscale garnet vein yields 2.42 ± 0.32 GPa at 635 ± 60°C. Zirconium-in-rutile thermometry applied to the same garnet vein provides a temperature of ~620°C. Altogether, the microchannels, microfractures and mesofractures represent migration pathways for fluids that were produced during glaucophane and lawsonite breakdown. The microfractures are likely precursors of the mesoscale fractures. These dehydration reactions indicate that high

OPEN ACCESS

Edited by:
Bernhard Grasemann, University of Vienna, Austria

Reviewed by:
Luca Menegon, University of Oslo, Norway
Simona Ferrando, University of Turin, Italy

***Correspondence:**
Michał Bukała
bukala@agh.edu.pl

Specialty section:
This article was submitted to Petrology, a section of the journal Frontiers in Earth Science

Received: *13 August 2020*
Accepted: *05 November 2020*
Published: *17 December 2020*

Citation:
Bukała M, Barnes CJ, Jeanneret P, Hidas K, Mazur S, Almqvist BSG, Kośmińska K, Klonowska I, Šurka J and Majka J (2020) Brittle Deformation During Eclogitization of Early Paleozoic Blueschist. Front. Earth Sci. 8:594453. doi: 10.3389/feart.2020.594453

pore-fluid pressure was a crucial factor for fracturing. Brittle failure of the eclogites thus represents a mechanism for fluid-escape in high-pressure conditions. These features may be directly associated with seismic events in a cold subduction regime.

Keywords: eclogitization, high-pressure brittle deformation, slab dehydration, pore-fluid overpressure, seismometamorphism

INTRODUCTION

High-pressure (HP) brittle deformation of subducting slabs has recently drawn increasing attention through petrological (e.g., Angiboust et al., 2012; Scambelluri et al., 2017; Behr et al., 2018), experimental (e.g., Okazaki and Hirth, 2016; Ferrand et al., 2017) and geophysical investigations (e.g., Kita and Ferrand, 2018; Florez and Prieto, 2019). HP brittle deformation is often correlated to an important facies change from blueschist to eclogite as it is coupled with significant metamorphic dehydration reactions (Peacock, 1993; Gao and Klemd, 2001; Hacker et al., 2003; Austrheim and Andersen, 2004). However, only a few natural examples of HP-low-temperature (LT) brittle failure have been reported (Gao and Klemd, 2001; Austrheim and Andersen, 2004; Angiboust et al., 2012; Deseta et al., 2014; Magott et al., 2016; Taetz et al., 2016, 2018). Several studies have recently emphasized the role of HP fractures as metamorphic fluid pathways allowing H_2O-rich fluids to migrate within the slab, drain fluids out of the slab (Gao and Klemd, 2001; Taetz et al., 2016; Angiboust et al., 2017; Taetz et al., 2018), and allow fluids from the underlying slab mantle to migrate upwards (Smit and Pogge von Strandmann, 2020). Such channelized fluid flow appears to be a key factor in slab metasomatism, affecting element transport as well as slab rheology (e.g., Smit and Pogge von Strandmann, 2020).

Although the high ambient pressure and temperature should inhibit brittle failure, natural studies clearly document brittle deformation at HP conditions (e.g., Austrheim and Boundy, 1994; Lund and Austrheim, 2003; John and Schenk, 2006; Angiboust et al., 2012; Incel et al., 2017; Scambelluri et al., 2017; Behr et al., 2018). Such deformation has been linked to seismicity in the subducting slab, which is strongly linked to either intermediate-depth earthquakes that concentrate along the upper and lower Wadati–Benioff planes (Hasegawa et al., 1978; Brudzinski et al., 2007; Florez and Prieto, 2019), or for episodic tremor and slow slip (ETS) events that occur downdip of the seismogenic zone in the subducting slab (Obara 2002; Rogers and Dragert, 2003). While these seismic events are significantly different, the locations of both intermediate-depth earthquakes and ETS events are strongly linked to the hydrated portions of the slab (Davies, 1999; Peacock, 2001; Hacker et al., 2003; Jung et al., 2004; Peacock, 2009; Fagereng and Diener, 2011; Hayman and Lavier, 2014; Audet and Kim, 2016; Wang et al., 2017). This spatial correlation may be a result of elevated pore-fluid pressure in the subducting rocks, allowing for brittle deformation to occur (e.g., Davies, 1999). More specifically, this has been linked to eclogitization of blueschists and decomposition of lawsonite and glaucophane by both laboratory and natural studies (e.g., Fagereng and Diener, 2011; Audet and Kim, 2016; Okazaki and Hirth, 2016; Taetz et al., 2016; Incel et al., 2017; Behr et al., 2018; Taetz et al., 2018). However, due to the relative scarcity of exhumed rocks recording a brittle failure at HP conditions, the exact relationships between dehydration reaction and deformation—with possible seismic implications—remain an open question.

Here, we present petrological and microstructural characteristics of eclogite bodies hosted within the Tsäkkok Lens of the Seve Nappe Complex (Scandinavian Caledonides). This study's main goal was to obtain an insight into the coupling between *in situ* dehydration at the blueschist to eclogite facies transitions, and the formation of the set of fractures on the oldest (early Paleozoic) documented natural example. The brittle structures of these rocks comprise microfractures related to the production of fluids during dehydration and mesofractures reflecting the fluid expulsion channels from the eclogites. Altogether, these eclogites demonstrate that dehydration during prograde eclogitization, reaching conditions of ~2.5 GPa and ~620°C, resulted in HP brittle deformation and fluid expulsion that are potentially related to deep seismicity in the subducting slab.

GEOLOGICAL SETTING

The Tsäkkok Lens, along with underlying Sarek and Vaimok lenses, belongs to the Seve Nape Complex, which constitutes the upper part of the Middle Allochthon of the Caledonian Orogen (e.g., Barnes et al., 2020 and references therein; **Figure 1**). These rocks represent a volcano-sedimentary succession developed at the outermost parts of the Baltica rifted margin, subducted in late Cambrian–Early Ordovician time (Kullerud et al., 1990; Root and Corfu, 2012). Some of the eclogites preserve pillow basalt fabrics (**Figure 2A**) and have a tholeiitic composition with E-MORB signature, indicating that they formed in an oceanic or ocean-continent transition environment (Kullerud et al., 1990). The eclogites are hosted in metapsammites, metapelites, calc-silicates and marbles (Kullerud, 1987).

The remnants of the subduction-related S1 foliation in the metasedimentary rocks is defined by interlayers of quartz-rich, calcite-rich and mica-rich lithologies. The S1 is locally preserved among the eclogite bodies where it was shielded from overprinting and transposition into the dominant exhumation-related foliation S2 (Barnes et al., 2020). In contrast, the eclogite pods predominantly behaved as rigid bodies. The bodies vary in length from a few centimeters to ≥250 m and are most often elongated parallel to the S2. The well-preserved pillow basalt fabrics clearly demonstrate they were not pervasively penetrated by ductile deformation during the entire evolution from

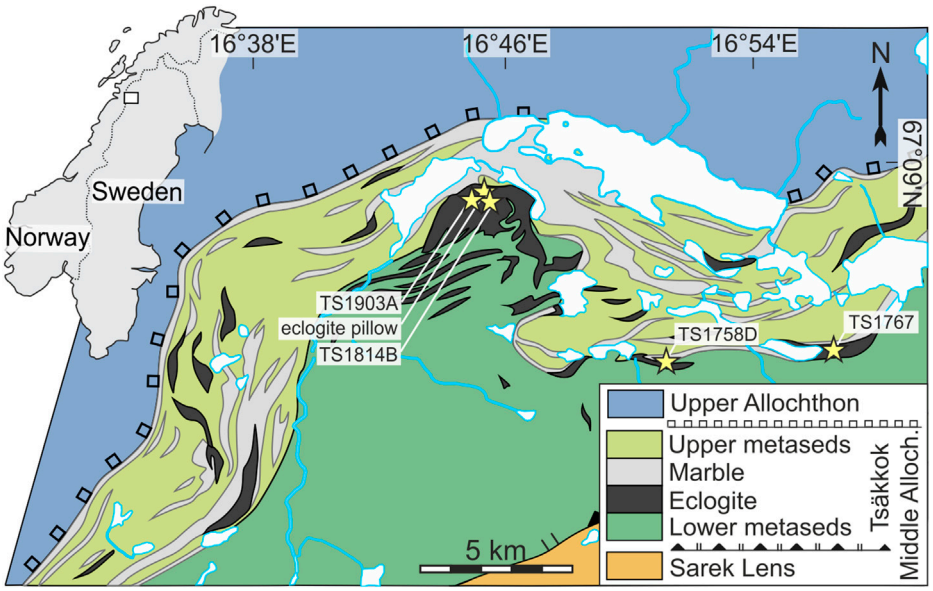

FIGURE 1 | A generalized tectonostratigraphic map of the study area (modified after Kullerud et al., 1987). Black lenses represent eclogite outcrops, whereas yellow stars mark the sampled ones. The detailed list of samples and GPS coordinates are provided in **Supplementary Table S1**.

subduction to exhumation (Barnes et al., 2020). The only evidence for ductile deformation in eclogite bodies is along their margins where retrogression under amphibolite/greenschist facies is coupled with foliation development concordant with the S2 (Barnes et al., 2020).

The Tsäkkok eclogites are typically believed to have undergone a metamorphic evolution from early amphibolite through blueschist to eclogite facies conditions with an overall HP assemblage demarcated by the presence of glaucophane and omphacite (Kullerud et al., 1990). The previous pressure–temperature (P–T) estimates obtained, based on a garnet-clinopyroxene geothermobarometry, suggest temperatures and minimum pressures of 500–630°C and 1.2–1.5 GPa, respectively (Kullerud et al., 1990 and references therein). Pioneering work to date the eclogite facies metamorphism using garnet + omphacite + whole rock Sm-Nd geochronology yielded an age of 505 ± 18 Ma (Mørk et al., 1988). However, the validity of this age has come into question with more recent zircon U-Pb geochronology that was applied to the eclogite bodies, providing an age of 482 ± 1 Ma (Root and Corfu, 2012). Regardless of the discrepancy for the age of eclogite facies metamorphism, both studies evince a late Cambrian/Early Ordovician metamorphic history for the Tsäkkok Lens.

MATERIALS AND METHODS

Sample Preparation

For this study, eclogite samples were obtained from the Tsäkkok Lens in the Norrbotten region of northern Sweden (**Figure 1**). The following representative samples have been chosen for the detailed investigation: phengite-bearing eclogite (sample TS1758D), phengite-free eclogite (sample TS1767), garnet vein (sample TS1814B; **Figure 2B**), and omphacite vein (sample TS19013A; **Figure 2D**). A detailed sample/outcrop list with GPS coordinates is provided in **Supplementary Table S1**. Standard 30 µm thin sections were prepared and polished with a 1 µm diamond paste. Thin sections used for EBSD analyses were additionally re-polished with <1 µm colloidal silica. Samples for X-ray computed microtomography analyses were prepared by cutting a ~1.5 cm^3 cube out of selected samples.

Electron Microprobe Analysis

Wavelength-dispersive spectroscopy (WDS) analysis of mineral chemistry was performed using a Jeol JXA8530F Hyperprobe electron probe microanalyser at the Department of Earth Sciences, Uppsala University (UU), Sweden and Jeol Superprobe 8230 electron microprobe at the Faculty of Geology, Geophysics and Environment Protection, AGH-University of Science and Technology (AGH-UST) in Kraków, Poland. Quantitative elemental analyses were performed with a 15–20 nA beam current and a 15 kV accelerating voltage, with counting times of 10 s on peaks and 5 s on background positions for silicates. The analyses of Zr in rutile were performed with an accelerating voltage of 15 kV and a beam current of 120 nA. The counting times were 150–300 s on peaks and 75–150 s on background positions. The beam size ranged from 1 to 15 µm depending on the mineral analyzed. Mineral reference materials and pure element synthetic oxides were used for calibration. All elements were analyzed using Kα spectral lines. Raw counts were corrected using the PAP routine (Pouchon and Pichnoir, 1988). The Jeol JXA8530F Hyperprobe (UU) was used to collect WDS X-ray concentration maps presented in **Figure 3**, using a 40 nA beam current, a 15 kV accelerating voltage and a 100 ms/pixel

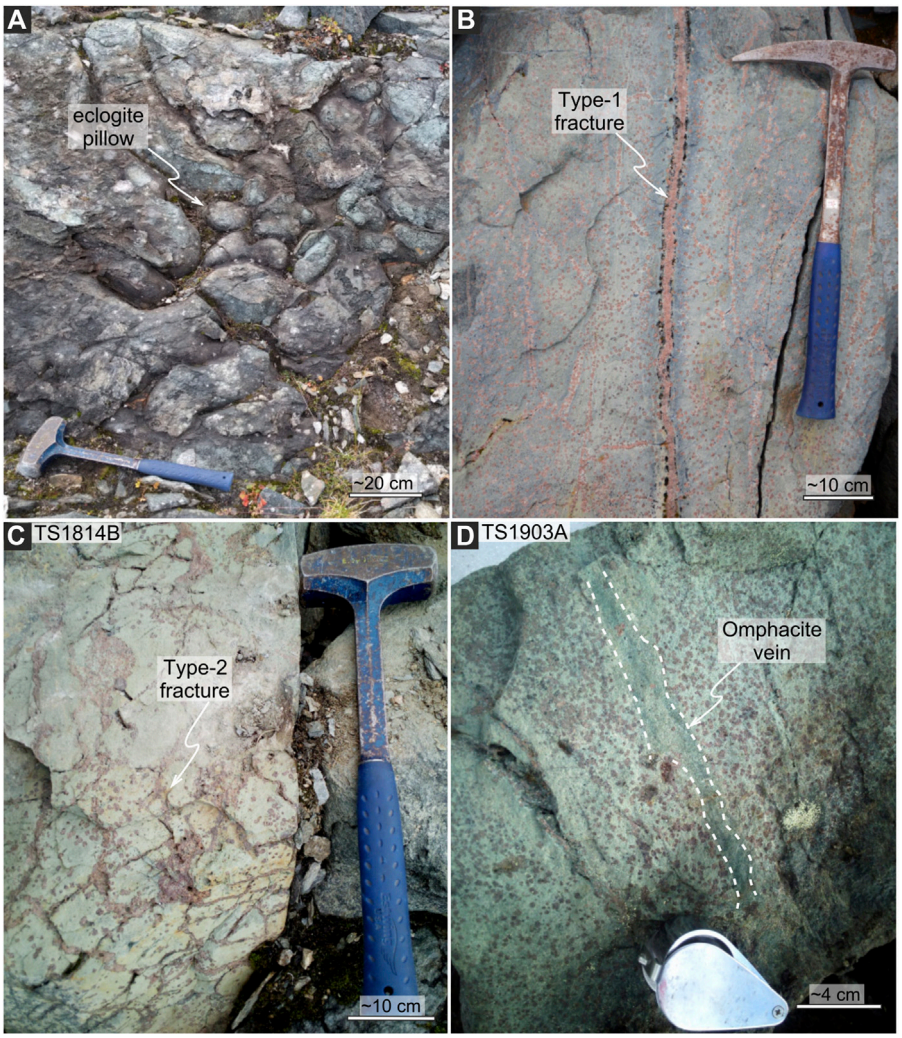

FIGURE 2 | Representative eclogite outcrops. **(A)** Eclogite pillow lava. **(B)** The Type-1 fractures, sealed by garnet, that are flanked by thinner, parallel fractures that are also sealed by garnet. **(C)** The Type-2 fractures, sealed by garnet, forming an interconnected network of sealed veins (sample TS1814B). **(D)** The omphacite-sealed fracture crosscutting a fine-grained eclogite (sample TS1903A). Hand lens for scale.

dwell time. The Jeol Superprobe 8230 (AGH-UST) was used to collect WDS X-ray concentration maps presented in **Figure 6**, using a 100 nA beam current, a 15 kV accelerating voltage and a 100 ms/pixel dwell time. Data treatment of WDS X-ray map was performed using the XMapTools v3.4.1 software (Lanari et al., 2014).

X-Ray Computed Microtomography

The 3D imaging was performed with a Phoenix v|tome|x L240 high-resolution computed microtomography system at the Earth Science Institute of the Slovak Academy of Sciences in Banská Bystrica. The investigated sample was analyzed by a 240 kV/320W microfocus tube. The sample was scanned with a 160 kV source voltage and a 125 μA current with 2200 projections and a nominal voxel size of 20 μm. The exposure time was 500 ms. After the scanning process, 3D data sets were evaluated with VG Studio Max 2.2 software. The surface determination and manual segmentation tools were used for extraction of selected grains.

Electron Backscatter Diffraction

Orientation mapping by electron backscatter diffraction (EBSD) was conducted under low vacuum (at 10 Pa) in a Zeiss EVO MA 15 Scanning Electron Microscope at the Instituto Andaluz de Ciencias de la Tierra (Armilla, Spain), which is equipped with an Oxford Instruments Nordlys Nano EBSD detector and Energy Dispersive X-ray Spectrometer (EDS). Instrumental settings were set to a 20 kV acceleration voltage, a 24 mm working distance and a probe current up to 500 pA. The acquisition conditions in the AZtec v. 3.1 (Oxford/HKL) data acquisition software module were 4 × 4 binning and a low (0) gain with a grid step of 1 μm. The percentage of indexed points in the raw maps exceeded 85% and only minor post-processing was necessary using the built-in functions of the Oxford/HKL Channel 5 software package by

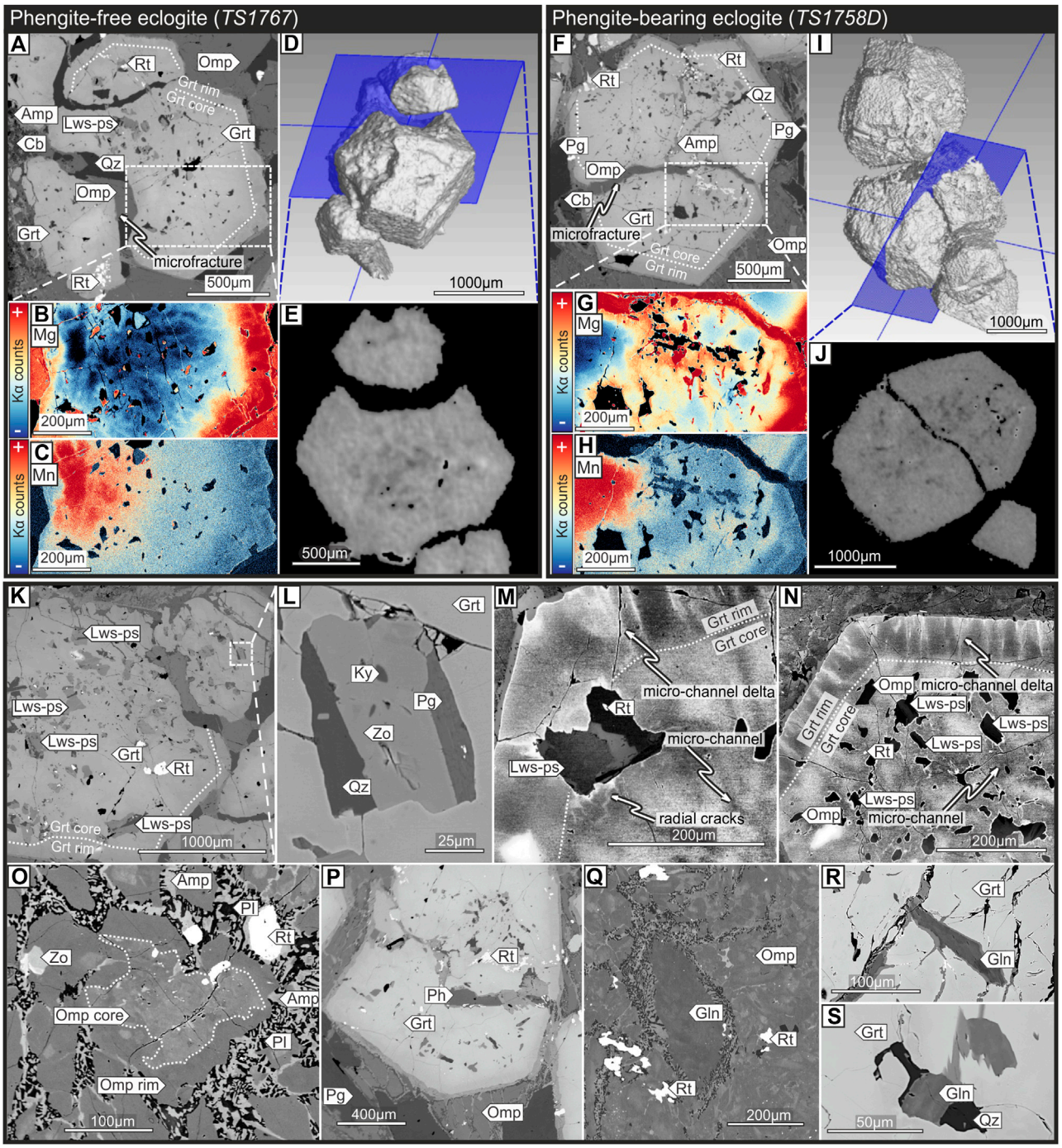

FIGURE 3 | Microstructural and petrographical features of eclogites. **(A and F)** Back-scattered electron (BSE) images of garnet with omphacite filling the fracture. **(B and G)** Wavelength-dispersive X-ray spectrometry (WDS) map of Mg. The garnet core exhibits a network of microchannels propagating towards the rim. **(C and H)** WDS map of Mn. **(D and I)** 3-dimensional model of fractured garnet obtained by μ-CT scanning eclogite samples. **(E and J)** 2-dimensional image intersecting garnet, obtained along the blue planes in picture D and I, respectively. Images A-E show a garnet from the phengite-free sample TS1767, whereas images F-J show garnet from the phengite-bearing sample TS1758D. **(K)** Fractured, subhedral-to-anhedral garnet porphyroblasts with an abundance of polyphasic mineral inclusions after lawsonite (sample TS1767). The white dashed line marks the garnet core/rim boundary. **(L)** Close-ups of polyphasic lawsonite pseudomorphs of rhomboidal shape. **(M)** High-contrast BSE image showing microchannels radially propagating outward from the polyphasic mineral inclusion (clinozoisite + quartz + paragonite + rutile). **(N)** High-contrast BSE image showing microchannels and microchannel deltas. **(O)** Zoned omphacite grain within eclogite matrix. **(P)** BSE images of garnet with phengite filling the fracture. **(Q)** Partially decomposed glaucophane in the eclogite matrix. **(R)** Glaucophane in a fracture within the garnet core. **(S)** Glaucophane inclusion within the garnet core. Images M and N were obtained by the "local equalization" filter which enhanced the contrast near image edges and reveals details in both light and dark regions of the BSE image. The filter uses 5 neighboring pixels to create a high-contrast effect. Mineral abbreviations: Grt, garnet; Omp, omphacite; Qz, quartz; Amp, amphibole; Lws-ps, lawsonite pseudomorph (clinozoisite + kyanite + quartz ± paragonite); Rt, rutile; Cb, carbonate; Ky, kyanite; Zo, clinozoisite; Pg, paragonite.

removing wildspikes and filling non-indexed pixels based on the orientations of the 8 neighboring pixels. Further data processing and calculations were accomplished using the built-in functions of the free MTEX 5.2.7 Matlab toolbox (mtex-toolbox.github.io; Hielscher and Schaeben, 2008; Bachmann et al., 2010). Grain reconstruction is accomplished using a segmentation angle of 12° between neighboring pixels. Misorientation maps (Mis2Mean) are calculated as the misorientation at each pixel of a grain relative to the grain's mean orientation. Inverse pole figure (IPF) maps are color-coded with respect to the x-vector (oriented horizontally along the plane of the section). Omphacite crystal shapes are plotted using the built-in "crystalShape" function of MTEX.

RESULTS

Investigation of the Eclogite Groundmass

Petrography and Mineral Chemistry

All of the studied Tsäkkok eclogites preserve an eclogite facies mineral assemblage of garnet + omphacite + rutile + quartz ± (Na–Ca)-amphibole ± phengite ± dolomite ± clinozoisite. Partially decomposed remnants of (Na)-amphibole (including glaucophane *sensu stricto*) are locally preserved within the matrix (**Supplementary Figure S1** and **Figure 3**). Garnet is typically found in clusters of 2-4 amalgamated grains surrounded by a single, continuous rim (**Figures 3A,B,F,G**). The cores exhibit prograde zoning with a rimward decrease of Fe ($Alm_{65–57}$) and Mn (Sps_{8-1}), coupled with Mg (Prp_{8-14}) enrichment (**Figures 3B,C,G,H**). Zoning of Ca is patchy but decreases slightly towards the rim ($Grs_{25–22}$) (**Supplementary Figures S2**, **S3**). The rims are characterized by homogeneous, high Mg content ($Alm_{50–51}Prp_{29–30}Grs_{18–20}Sps_1$), however, garnet rims occasionally show distinct oscillations of Mn (**Figure 3H**). Additionally, both garnet core and rim chemical zoning is in some places disturbed by microchannels and microfractures. The rims and the outermost parts of the garnet core contain sparse omphacite and rutile inclusions. In contrast, the inner cores of the garnet contain abundant inclusions of quartz, (Na)-amphibole, (Na-Ca)-amphibole and up to 250 μm long, mineral inclusions that are rhombohedral in shape which consist of clinozoisite + quartz ± kyanite ± paragonite (**Figures 3K–N** and **Supplementary Figure S4**). Matrix-located omphacite cores (Jd < ~43 mol%) display patchy Fe zoning in contrast to the omphacite rim (Jd > ~43 mol%), which is relatively depleted in Fe (**Figure 3O**). Phengite forms flaky grains in the matrix and within the garnet fractures (Figure 3P), not exceeding 300 μm in length, with an Si content of 3.30–3.39 a.p.f.u (**Supplementary Table S2**).

Microscale Fracturing and Garnet Microstructures

Comparison of the chemical composition and the 3D shape reconstruction of the garnet porphyroblasts shows a cluster of garnet cores enveloped by a single, continuous rim. Back-scattered electron images (BSE) and Wavelength Dispersive X-ray Spectrometry (WDS) maps of garnet from phengite-bearing and phengite-free eclogite types (**Figure 3**), reveal a network of microchannels. These microchannels show a remarkably different composition (Mg-rich) from that of the primary garnet (**Figures 3, 4**), have diffuse boundaries and propagate outward from the polyphase inclusions, penetrating both the cores and rims of the porphyroblasts. Within the garnet rims, the micro-channels fan out toward the grain boundaries, creating microchannel "deltas" (**Figures 3M,N**). Within the same volumes, garnet has a few, relatively poorly defined orientation domains delimited by low-angle (<3°) boundaries (**Figure 4**), and it also hosts widely spaced, <1 μm-wide hairline fractures (see Hawemann et al., 2019). The intracrystalline misorientation maps show that within the orientation domains, the garnet grain interiors are virtually undeformed with very low (<0.5°) local internal misorientations (**Figures 4C,H**). The most prominent low-angle boundaries occur at the borders of the orientation domains with misorientations in the range of 1.5°–3° and have curvilinear shapes (**Figures 4B,G**). Misorientation profiles across these low-angle boundaries show no progressive distortion of the crystal lattice but a sudden jump in misorientation (**Figures 4D,I**). The low-angle boundaries are sharp toward the edges of the porphyroblasts, while they become rather diffuse in grain interiors due to a coreward diminution of the intragranular misorientation (e.g., **Figure 4D,I**). The misorientation axis distribution along both types of low-angle boundaries is apparently random, but the very low misorientation values impede the detailed analysis. Finally, low-angle boundaries usually occur without affecting the structural integrity of the crystals but in a few cases, they correlate with hairline fractures. Comparison of crystal orientation maps to BSE images demonstrates that the most penetrative internal low-angle boundaries and some of the hairline fractures are correlated to the location of Mg-rich garnet microchannels.

Larger-scale microfractures through both cores and rims of amalgamated garnets are readily observed. These fractures are up to 300 μm in width and are not observed to propagate into the adjacent omphacite matrix (**Figures 3A,F**). Reconstructed 3D shapes of the separated garnet fragments in both the phengite-bearing (sample TS1758D) and phengite-free (sample TS1767) eclogites indicate no offset along fractures (**Figures 3D,E,I,J**). The widest microfractures often record fluid-assisted omphacite ± quartz ± phengite ± clinozoisite crystallization (**Figures 3A,F,P**). Noteworthy, the composition of omphacite (Jd > 43 mol%) sealing microfractures is alike the composition of the rim of the omphacite porphyroblast located in the matrix (**Supplementary Table S2**).

Investigation of Mesoscale Fracturing of Eclogite Bodies

Garnet-Sealed Mesofractures

Mesoscale (cm-scale) fracturing is prominent in eclogite bodies. Locally, the omphacite-dominated groundmass is transected by garnet-sealed mesofractures. Two types of fracturing can be described within an individual eclogite body. The first type (hereafter referred to as "Type-1") is represented by straight mesofractures that can be tracked for more than 1 meter, with thicknesses up to 5 cm. These fractures are associated with thinner, equally pervasive sub-parallel fractures that are also sealed by garnet (**Figure 2B**). The second type (hereafter referred to as "Type-2") is an interconnected network of high-

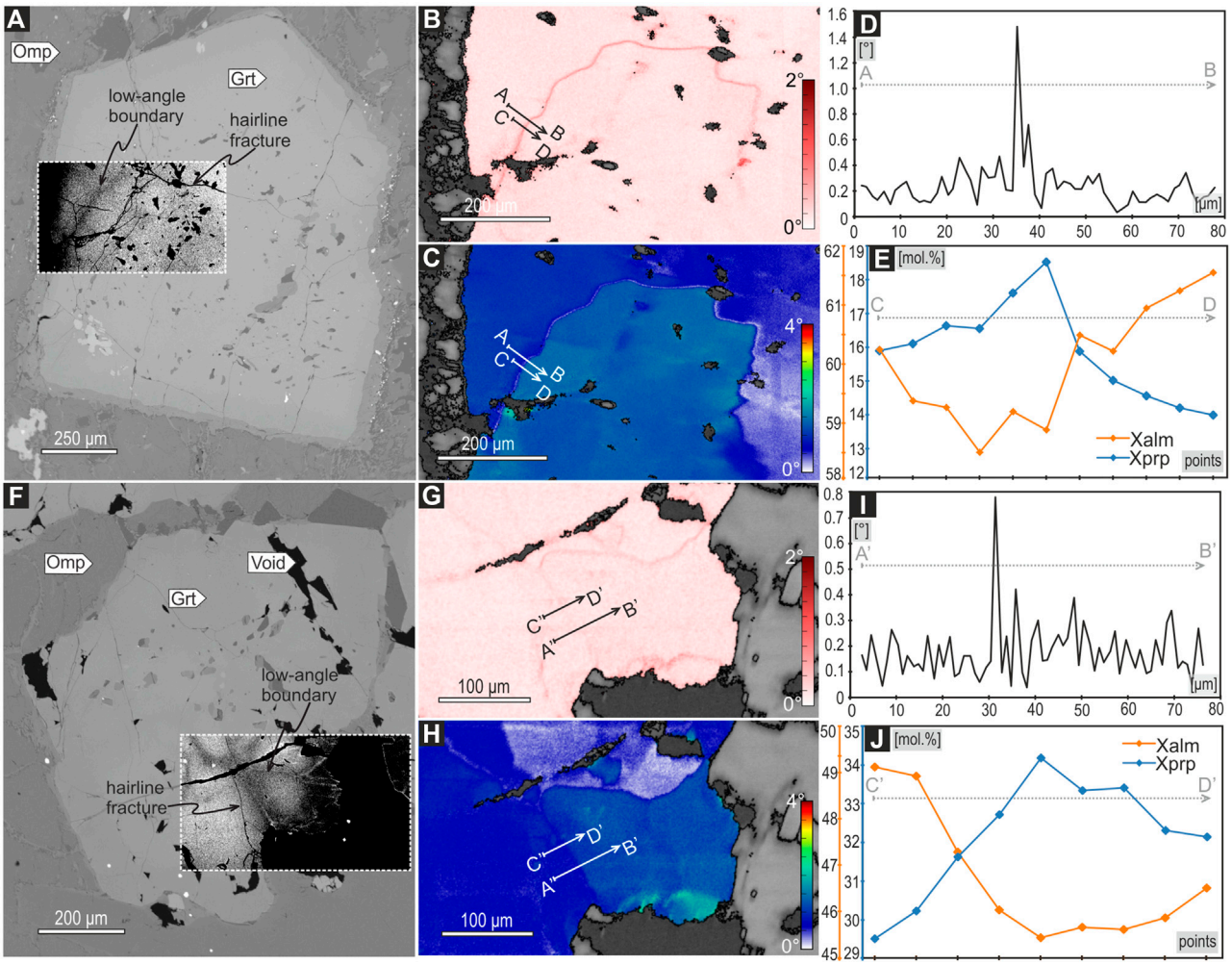

FIGURE 4 | Microstructures of representative garnet grains displaying misorientation along the microchannels. **(A and F)** BSE images of garnet grains. Inset high-contrast BSE images emphasize microchannels of different composition. **(B and G)** Electron backscatter diffraction (EBSD) maps of second nearest-neighbor Kernel Average Misorientation (2nd order KAM). **(C and H)** EBSD maps of intracrystalline misorientation, expressed as misorientation relative to the mean orientation of a grain, showing distortion along the micro-channel. **(D)** The misorientation profile (A→B) marked on images B and **C**. Misorientation does not exceed 1.5°. **(E)** The chemical profile (C→D) shows a distinct enrichment in X_{prp} (Mg) and depletions in X_{alm} (Fe). Note that *y*-axis values are different for each garnet endmember. **(I)** The misorientation profile (A′→B′) marked on images G and **H**. Misorientation does not exceed 0.8°. **(E)** The chemical profile (C′→D′) shows an enrichment in X_{prp} (Mg) and depletions in X_{alm} (Fe). Mineral abbreviations: Grt, garnet; Omp, omphacite.

angle mesofractures that define angular fragments of eclogite, up to 30 cm in diameter (**Figure 2C**).

The garnet veins are dominated by dense garnet clusters (>95 vol%; sample TS1814B; **Figures 5A,B**). Regardless of the thickness of veins, two distinct zones can be observed (**Figures 5B,C,D**). The inner zone, despite the patchy Ca zoning, displays minor variations of other elements and preserves a composition of $Alm_{60-64}Grs_{22-27}Prp_{7-10}Sps_{6-8}$ (**Figure 5C,D**; **Supplementary Table S3**). The garnet contains numerous inclusions of omphacite, glaucophane, rutile, quartz, clinozoisite, zircon and chlorite as well as the inclusions of associated clinozoisite + quartz ± paragonite. Composition of omphacite within the inner zone varies over a narrow range (Jd = 46–49 mol%, Aeg = 9–12 mol%). The change from the inner to the outer zone is marked by a decrease in the number of inclusions and a sharp change in garnet chemistry (**Figures 5 and 6C,D**; **Supplementary Figures S5, S6**; **Supplementary Table S3**). The outer zone displays a rimward decrease of Fe (Alm_{66-58}) coupled with Mg increase (Prp_{11-22}) and relatively flat Ca (Grs_{19-22}) and Mn ($Sps_{<2}$) content. In addition, garnet within the outer zone display oscillatory Mn zoning (**Figure 5D**). The garnet within the outer zone of garnet veins contains inclusions of rutile + omphacite + quartz ± paragonite. The omphacite composition is quite uniform (Jd = 48–49 mol%, Aeg = 8–12 mol%). Notably, scarce quartz domains can be found within the garnet veins, which contain euhedral omphacite grains growing inwards from the domain edges (**Supplementary Figure S6**).

Detailed microstructural and chemical mapping by EDS-EBSD revealed that the high-Mn inner zone of the garnet vein is disrupted and sealed. The disrupted zone of the garnet vein is sealed by low-

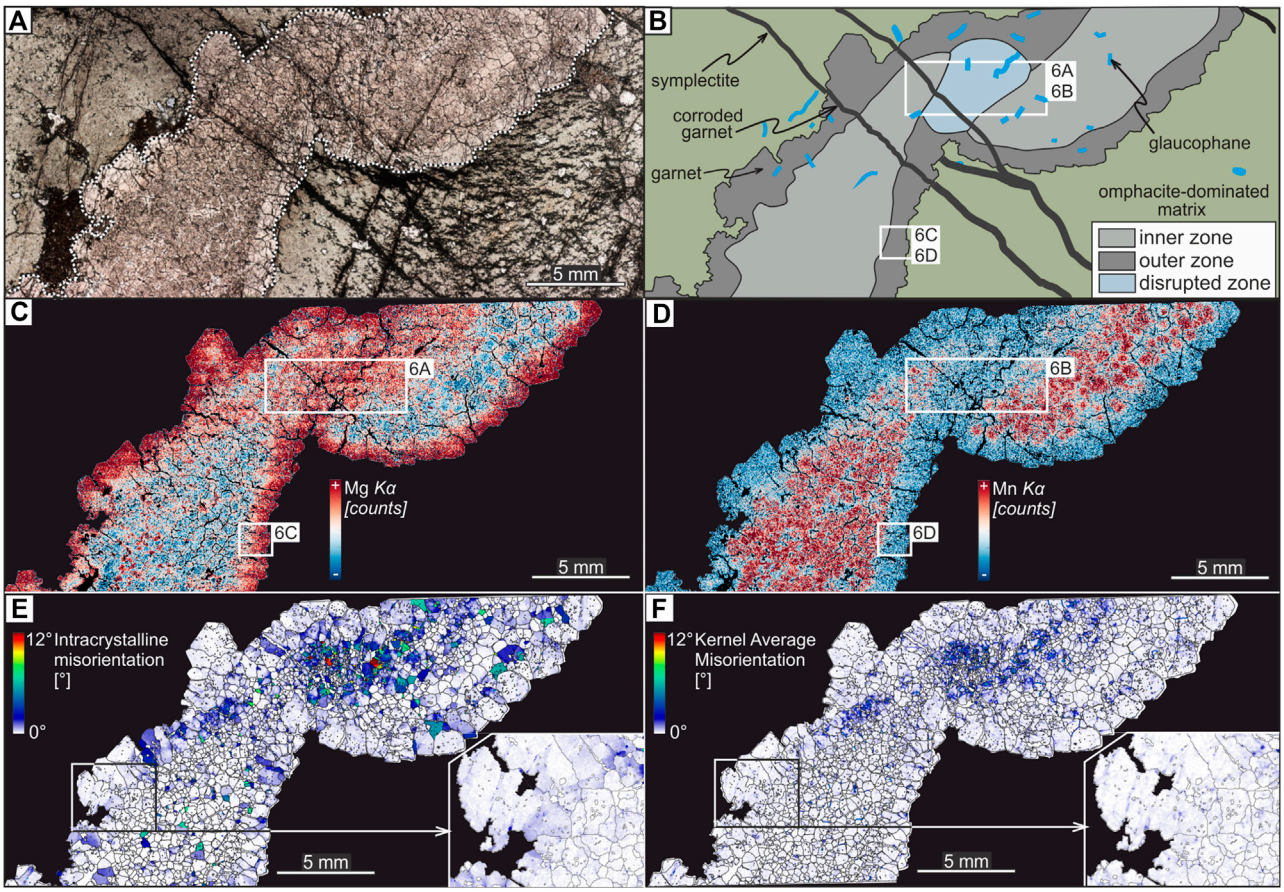

FIGURE 5 | The microstructure and chemical composition of a Type-2 garnet vein. **(A)** Thin section scan (plane polarized light) showing a garnet vein propagating through finer-grained, omphacite-dominated groundmass. **(B)** Illustrative interpretation of the thin section scan showing the internal structure of garnet vein. White rectangles areas with qualitative WDS maps. **(C)** EDS map of Mg within the whole garnet vein. **(D)** EDS map of Mn within the whole garnet vein. **(E)** EBSD map of intracrystalline misorientation within the whole vein–expressed as misorientation relative to the mean orientation of a grain–showing higher strain in the disrupted zone. **(F)** EBSD maps of second nearest-neighbor Kernel Average Misorientation (2nd order KAM).

Mn garnet and contains interstitial omphacite + quartz + glaucophane + phengite + rutile (**Figures 5C,D and 6E–I**). Unlike the inner and outer zone, numerous apatite grains are present in the disrupted zone (**Figure 6I**). Omphacite within the disrupted zone shows a composition of Jd = 47–50 mol%, Aeg = 9–11 mol%, which encompasses the same compositional range of the omphacite analyzed within the inner and outer zones. Phengite contains up to 3.36 Si a.p.f.u. The chemical composition of garnet sealing the disruption zone is highly heterogeneous and shows sharp variations on the ten-micron scale (**Figures 6A,B**). Despite the chemical variations, garnet displays an overall high-Mg, the low-Mn composition of approximately $Alm_{56–58}Grs_{21–22}Prp_{18–21}Sps_{<2}$ (**Figures 6A,B** and **Supplementary Figures S7**, **S8**), resembles the composition of the outer zone.

Garnet throughout the entire vein shows little elongation and minor intracrystalline substructure that is defined by slight changes in orientation without clear subgrain boundaries (**Figures 5E,F**). By contrast, garnets of the disrupted zone display grain size reduction and a high density of sharp, intracrystalline misorientations in equant grains (**Figures 6J–L**). Furthermore, garnet in this zone shows serrated grain boundaries, which contrasts with the straight to moderately curvilinear grain boundaries, and euhedral shapes of the bigger grains within the vein.

Sets of prominent retrograde microfractures transect the mesofractures. These microfractures are pervasive throughout garnet cores and rims and penetrate the omphacite groundmass. Garnet is partially corroded along these fractures that are predominantly filled with calcite + iron oxides, whereas omphacite adjacent to the fractures has decomposed to amphibole (pargasite and actinolite) + plagioclase + quartz symplectites (**Figures 5A,B**).

Omphacite-Sealed Mesofractures

Locally, the eclogite groundmass is crosscut by omphacite-sealed fractures (sample TS1903A; **Figure 2D**). The mineral composition of these veins is dominated by omphacitic clinopyroxene (>98 vol%) with a minor amount of apatite and quartz (**Figure 7**). The omphacite that seals vein consists of highly elongated grains (up to 1.5 mm in length), with elongation

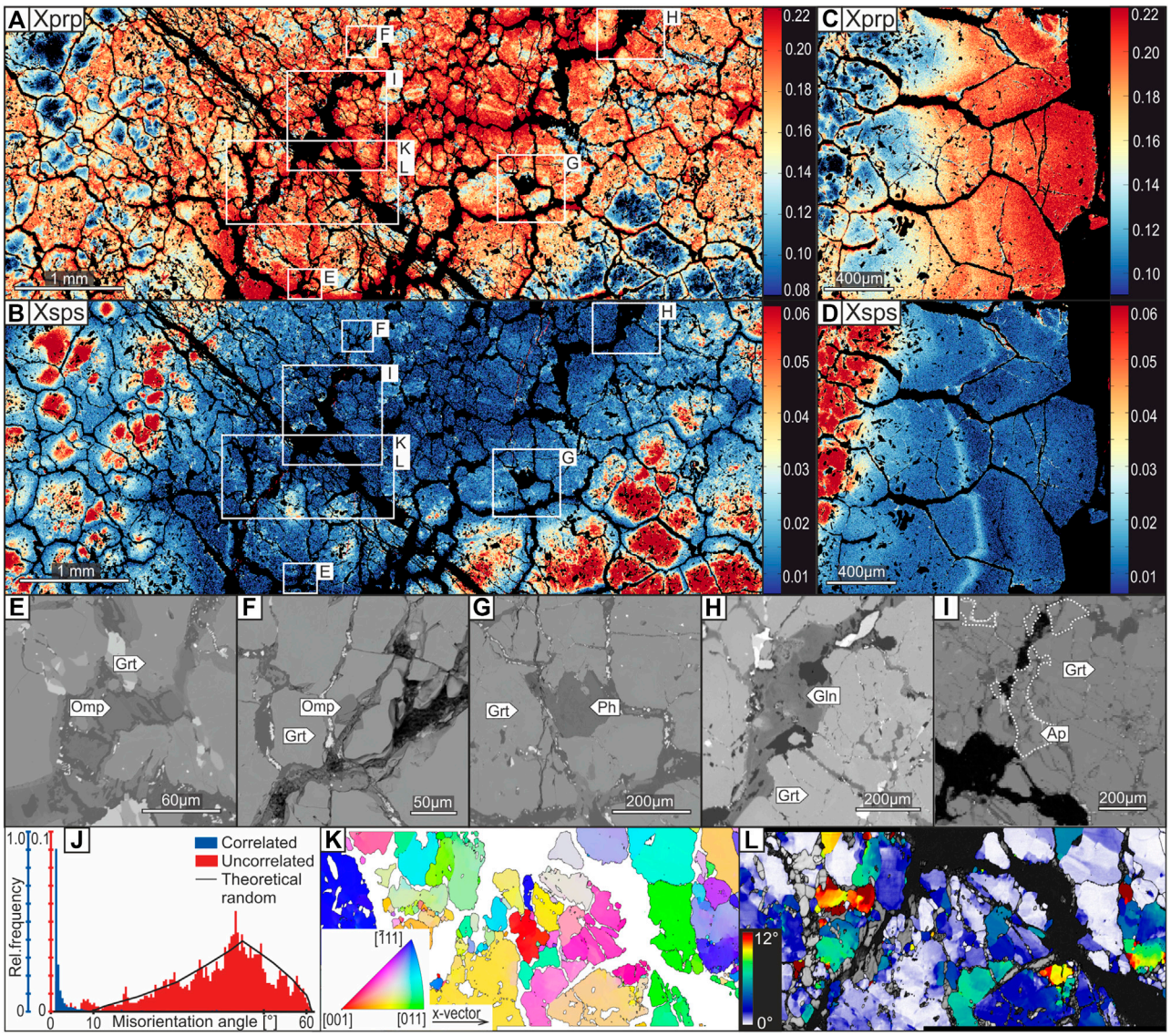

FIGURE 6 | (A and B) Standardized WDS maps of pyrope (Xprp) and spessartine (Xsps) endmembers in the disrupted zone, respectively. **(C and D)** Standardized WDS maps of pyrope (Xprp) and spessartine (Xsps) endmembers along the boundary of the inner and outer zone. **(E and F)** BSE images of omphacite, **(G)** Phengite, **(H)** Glaucophane, **(I)** Apatite that is located in the disrupted zone. **(J)** Histogram of distribution of misorientation angles for garnet in the disrupted zone, presented on the images K and L. Distribution is dominated by low-angle values for correlated pairs. Note, that *y*-axis on the diagram has different values for correlated and uncorrelated pairs. **(K)** EBSD map showing the garnet orientation using inverse pole figure coloring in reference to the x-vector. **(L)** EBSD map of intracrystalline misorientation of garnet. Mineral abbreviations: Grt, garnet; Omp, omphacite; Ph, phengite; Gln, glaucophane, Ap, apatite.

directions along [001] crystal axis and shape preferred orientation (SPO) subnormal to the vein walls (**Figure 7A**). Locally, omphacite is retrogressively overgrown by amphibole + plagioclase + quartz symplectites, not exceeding 30 µm in width. Apatite forms rare, yet large grains up to 2.5 mm in diameter (**Figure 7B**). Omphacite chemical composition varies over a broad range and zoning changes chaotically within the grain, yet it approximately follows the general pattern identified in the matrix omphacite in the eclogite groundmass. In general, omphacite cores are characterized by a composition of $Jd_{<42}$ (X_{Mg} [Mg/(Mg + Fe^{2+})] = 0.52–0.69), which gradually changes to $Jd_{>42}$ (X_{Mg} = 0.70–0.78) in the omphacite rim. However, the low-Jd omphacite cores are also crosscut by a dense network of the (sub) micron high-Jd microchannels (**Figures 7C–E**).

P-T Conditions of Brittle Deformation

Conventional Geothermobarometry

The P–T conditions have been calculated for the garnet + omphacite + phengite assemblage from the eclogite sample TS1758D and the garnet vein sample TS1814B. The coupled method of garnet–clinopyroxene Fe^{2+}-Mg exchange thermometer (Ravna, 2000) and net-transfer reaction 6diopside + 3muscovite = 3celadonite + 2grossular + pyrope geobarometer (Ravna and Terry, 2004) have been used. For the

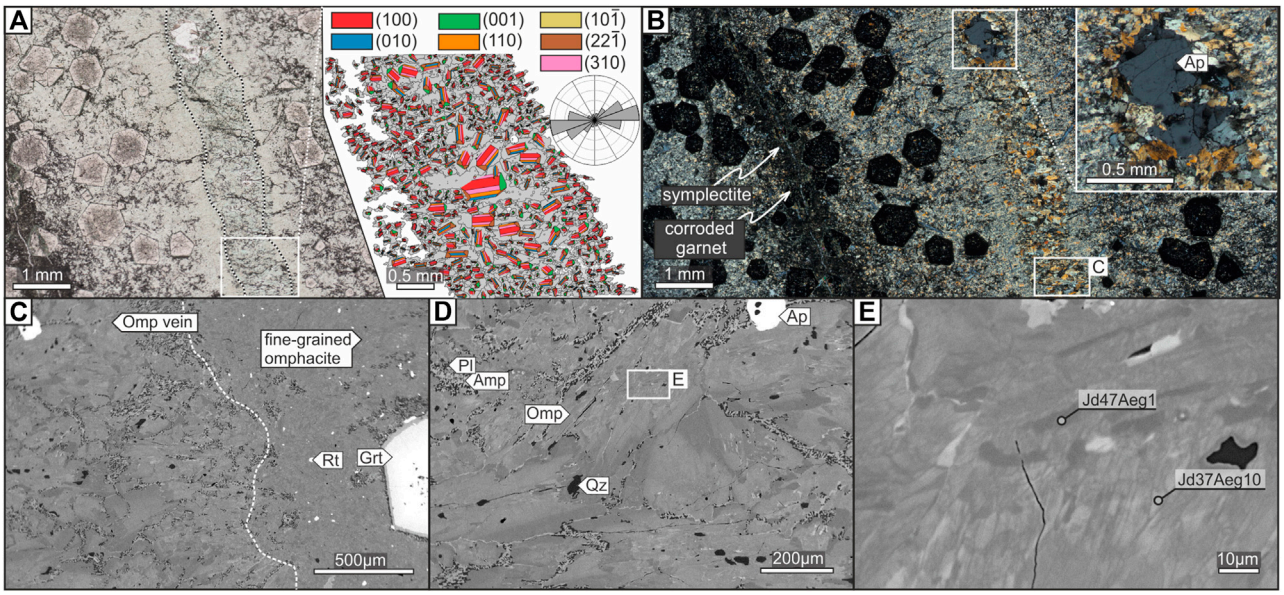

FIGURE 7 | The microstructure and chemical composition of omphacite vein. **(A)** Thin section scan (plane polarized light) of omphacite vein. The inset EBSD map shows omphacite grains with superposed ideal clinopyroxene crystal shapes reflecting the crystallographic orientation of each omphacite grain. The size of crystal shape drawing is proportional to the area of the corresponding grain in the map. Note that most omphacite grows perpendicular to the vein wall along [001] axes. Rose diagram shows an orientation of long axes of elongated omphacite grains, which are perpendicular to the vein boundary. **(B)** Thin section scan (crossed polarized light). Inset microphotograph shows apatite grain within the vein. **(C)** BSE image of the omphacite vein boundary (dashed line). **(D)** BSE image of large omphacite grains within the vein, displaying a chemical zoning. **(E)** Close-up BSE image of omphacite core, showing a highly irregular dense network of microchannels of high-Jd composition. Mineral abbreviations: Omp, omphacite; Rt, rutile; Grt, garnet; Pl, plagioclase; Amp, amphibole; Ap, apatite.

calculations, the following models have been used: 1) the garnet activity model by Ganguly et al. (1996), 2) the clinopyroxene activity model by Holland (1990) and 3) the phengite activity model and solid solution by Holland and Powell (1998).

In order to estimate the P-T conditions of the microscale fracturing, the following composition of minerals from sample TS1758D has been taken, i.e., 1) phengite with the max. Si (a.p.f.u) content, sealing fracture in garnet (**Figure 3P**), 2) omphacite with the max. jadeite (mol%) content, sealing fracture in garnet (**Figure 3F**), and 3) garnet along the micro-channel at the contact with phengite (**Figure 3F** and **Supplementary Table S2**). The results of this conventional geothermobarometry method yielded the P–T conditions of 2.47 ± 0.32 GPa at 620 ± 60°C (**Figure 8A**).

To estimate the P-T conditions of the mesoscale fracturing, the composition of minerals from sample TS1814B (Type-2 vein) located within the disrupted zone has been used, i.e., (1) the average composition of phengite, (2) the average composition of omphacite, and (3) the most frequent composition of a high-Mg garnet sealing the disrupted zone, calculated based on the WDS X-ray maps (**Figure 6**). The chemical composition of omphacite, and especially garnet sealing the disrupted zone varies over a broad range (**Figure 6** and **Supplementary Figures S7**, **S8**). Provided the highly irregular internal structure of the disrupted zone, the textural observations do not provide sufficient evidence to link a specific omphacite composition with garnet of a specific composition to have been formed in equilibrium. To avoid miscalculation caused by, e.g., erroneous or biased pairing of the omphacite with the garnet compositions, the most frequent composition of garnet and the average omphacite and phengite compositions have been used (**Supplementary Figure S8** and **Supplementary Table S3**). The results of the conventional geothermobarometry method yield the P-T conditions of 2.42 ± 0.32 GPa at 635 ± 60°C (**Figure 8A**). The assemblage of garnet, omphacite, and phengite provides reliable pressure estimates, but the temperature may be overestimated due to an uncertainty of the Fe^{2+}/Fe^{3+} ratio in clinopyroxene (Ravna and Paquin, 2003). Differences in P-T values obtained from eclogite (sample TS1758D), and the garnet vein (sample TS1814B) are minor and confirm the HP-LT conditions of brittle failure. The results plot within the eclogite facies along a cold subduction gradient of ~8°C/km (i.e., ~250°C/GPa; **Figure 8A**).

Trace Element Geothermometry

Zirconium in rutile (Zr-in-Rt) thermometry has been used to estimate the temperatures for the garnet vein formation/opening and to verify the P-T estimates provided by the conventional geothermobarometry (sample TS1814B), as the Zr-in-Rt method is independent from the major-element exchanges. The temperature of vein formation should be preferentially recorded by rutile inclusions in garnet, which are supposed to reflect entrapment temperature (e.g., Tomkins et al., 2007). However, there is no difference between measured Zr content in rutile inclusions and interstitial rutile located between garnet grains. In order to capture the presumed temperature variations between different zones, rutile grains from both the inner, outer, and disrupted zones have been analyzed (**Figure 5**). Rutile is not overgrown by titanite, but in some cases shows exsolutions of ilmenite. Measured Zr content in rutile

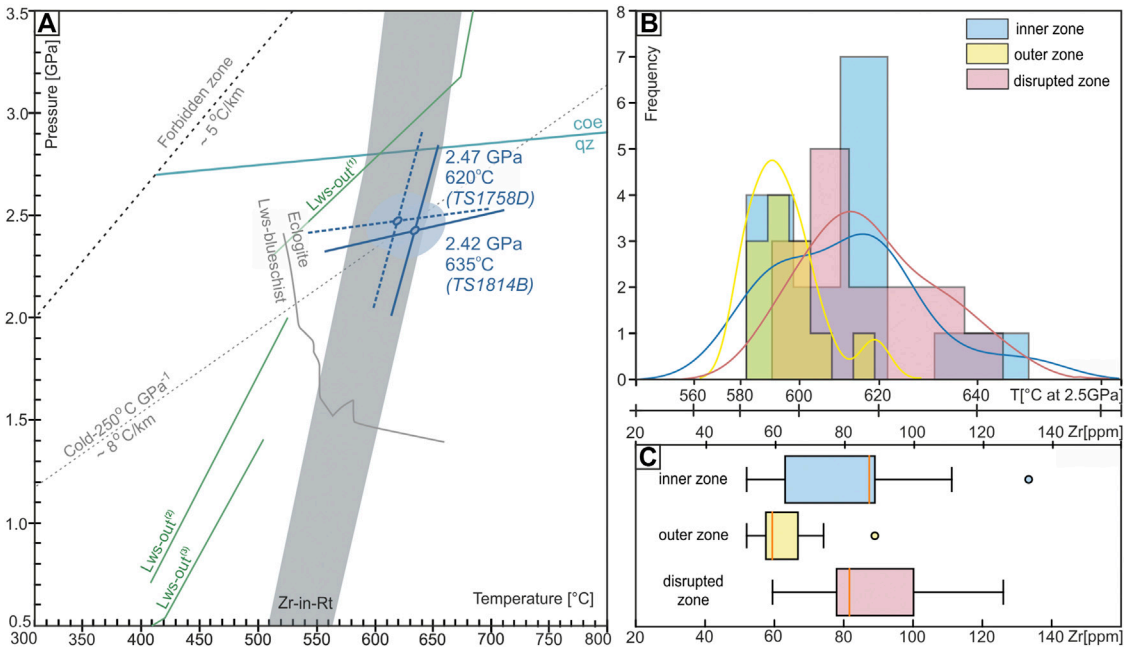

FIGURE 8 | (A) Pressure–temperature (P–T) diagram showing the results from the Tsäkkok Lens eclogites. Blue lines show a result of the applied geothermometer (Ravna, 2000) and geobarometer (Ravna and Terry, 2004). The dotted lines represent a geothermobarometric results for crystal-scale fracturing in the sample TS1758D, whereas the solid lines shows results for garnet vein in the sample TS1814B. The error of the estimates (i.e., ± 0.32 GPa and ±60°C) is represented by the ellipse. The gray field "Zr-in-Rt" shows the temperature range for garnet vein obtained by trace elements thermometry. This field encompass the results from inner, outer and disrupted zone of garnet vein. The lawsonite-blueschist to eclogite facies boundary, following the calculations of Palin and White (2016). The lawsonite breakdown reaction following the calculations of: Lws-out(1) (Schmidt and Poli, 1998), Lws-out(2) (Heinrich and Althous, 1988), Lws-out(3) (Newton and Kennedy, 1963). **(B)** Histogram of Zr content in rutile from each zone of garnet vein. Solid lines represent a Kernel Density Estimate (KDE) derived from each population. Note that the first *x*-axis shows a temperature (°C, at fixed pressure of 2.5 GPa), while the second *x*-axis shows a Zr content (ppm). **(C)** Box plot showing analyzed Zr distribution within each population.

from inner zone varies over 52–133 ppm (n = 15, av. = 81 ± 21 ppm; **Figure 8B**), the outer zone varies over 52–88 ppm (n = 12, av. = 63 ± 11 ppm), and in rutile from disrupted zone varies from 59 to 125 ppm (n = 15, av. = 88 ± 19 ppm; **Figure 8B** and **Supplementary Table S4**). Temperatures were calculated based on the pressure-dependent calibration provided by Tomkins et al. (2007) using the *a*-quartz stability field equation. Using a fixed pressure of 2.5 GPa, the temperature range obtained for the inner zone is 583–649°C, the outer zone is 583–619°C, and the disrupted zone is 592–645°C (**Figure 8B**). The temperature differences between the zones are minor and all show a concise temperature range of 583–649°C with a peak at 620 ± 34°C (2σ error; **Figure 8B**). Noteworthy, since the pressure of inner zone formation cannot be estimated, and the Zr-in-Rt temperature is provided for the pressure of 2.5 GPa, the result of ~583°C is most likely overestimated.

DISCUSSION

Prograde Dehydration

The remnants of glaucophane in the eclogite groundmass provide direct evidence for glaucophane decomposition during eclogitization. Within garnet porphyroblasts, the rhombohedral shapes of the inclusions, as well as the modal composition of clinozoisite + quartz ± kyanite ± paragonite, testify that they represent products of lawsonite breakdown (e.g., Fry and Fyfe, 1969; Bearth, 1973; Fry, 1973; Ballèvre et al., 2003; Angiboust and Agard, 2010; Orozbaev et al., 2015) similar to the lawsonite pseudomorphs reported from numerous lawsonite-eclogite localities (e.g., Ravna et al., 2010; Philippon et al., 2013; Ren et al., 2017). The phase composition of the lawsonite pseudomorphs can be explained by the simple lawsonite breakdown reaction (1) (Newton and Kennedy, 1963; Crawford and Fyfe, 1965; Liou, 1971):

$$4Lws = 2Zo + Ky + Qz + 7H_2O \quad (1)$$

However, pseudomorphs containing paragonite imply the presence of a Na-bearing phase involved in the lawsonite breakdown reactions. The phenomenon can be explained by three reactions that occur during the eclogitization of blueschists, involving simultaneous albite, jadeite and glaucophane breakdown (e.g., Heinrich and Althaus, 1988):

$$4Lws + Ab = 2Zo + Pg + 2Qz + 6H_2O \quad (2)$$

$$4Lws + Jd = Pg + 2Zo + Qz + 6H_2O \quad (3)$$

$$12Lws + 1Gln = 2Pg + 1Prp + 6Zo + 5Qz + 20H_2O \quad (4)$$

Notably, **Eq. (4)** is a garnet-forming reaction, which produces pyrope along with lawsonite pseudomorphs-defining phases. The

production of pyrope, the Mg-rich garnet endmember during eclogitization is in agreement with the composition of garnet rims and microchannels since they both display Mg enrichment (Prp up to 34 mol%) compared to the primary garnet core composition (Prp ≈ 8–14 mol%; **Figures 3B,G and 4E,J**). A relative enrichment in Mg is also indicative for the omphacite-sealed mesofracture (**Figure 7**) since the omphacite rim formed via fluid facilitated dissolution-reprecipitation has a X_{Mg} = 0.70–0.78 compared to the X_{Mg}= 0.52–0.69 measured in the omphacite core. The lawsonite breakdown reactions and decomposition of glaucophane in the eclogite groundmass attests to production of fluids due to the dehydration reactions during eclogitization. The sealing of the microscale fractures also strongly suggests the presence of fluids within the eclogite rock volumes. Furthermore, the chemical oscillatory Mn zoning observed in both single garnet grains in eclogites (**Figure 3H**) and the outer zone of garnet vein (**Figure 6D**) represent multiple garnet growth-resorption cycles that have been linked either with fluctuations in P–T during tectonic burial (García-Casco et al., 2002) or fluid influx (Whitney et al., 1996). Recent investigations also have shown that such a zoning could possibly form due to seismic-related pressure pulses affecting garnet stability (Viete et al., 2018).

High-Pressure Brittle Deformation in the Tsäkkok Eclogites

The texture of the Tsäkkok eclogites is dominated by mm-sized euhedral garnet porphyroblasts that are distributed homogeneously in an overall undeformed fabric and have equant crystal shapes, straight grain boundaries, as well as show integrity of the crystalline structure across low-angle boundaries (**Figures 3 and 4**). These microstructural features preclude that diffusion creep (e.g., Storey and Prior, 2005; Smit et al., 2011; Stünitz et al., 2020), cataclastic flow (e.g., Trepmann and Stöckert, 2002), or grain/phase boundary sliding (e.g., Terry and Heidelbach, 2004) were at play during the formation of garnet crystal substructures. The brittle–ductile transition in garnet occurs at temperature >600°C (Voegelé et al., 1999; Wang and Ji, 1999; Mainprice et al., 2004) and the high mechanical strength of garnet (e.g., Ando et al., 1993; Ingrin and Madon, 1995) can be significantly weakened at the presence of water, content of which in garnet can increase with pressure up to 3 GPa (Xu et al., 2013). Despite that, it is unlikely that Tsäkkok eclogites record the onset of crystalplastic deformation in hydrolytically weakened garnets at the peak metamorphic conditions (~620°C and 2.5 GPa). The absence of progressive lattice distortion towards low-angle boundaries (**Figures 4C,D,H,I**), the random crystallographic axes accommodating the low-angle misorientations (not shown), the scarcity of low-angle boundaries in the garnet structure (**Figures 4B,G**), and the lack of evidence for dynamic recrystallization at the edges of euhedral porphyroclasts (**Figures 4A,F**) imply that dislocation mobility cannot be responsible for the formation of low-angle boundaries in garnet. The undeformed grain interiors and the overall shape of garnet orientation domains rather indicate that low-angle boundaries represent minor misorientations along coalescence planes formed during amalgamation of garnet cores, which have been preserved and slightly accentuated towards the rims in subsequent overgrowth (see rimward sharpening of boundaries in **Figure 4B**). Alternatively, the low angle boundaries may represent healed microcracks in garnet with incompletion of the process along hairline fractures. In either case, at the peak metamorphic conditions of the Tsäkkok eclogite, garnets were dominantly brittle.

The network of microchannels in the garnet of Tsäkkok eclogite, proceeding to the micro-channel deltas along the rims, are similar to those previously reported from HP rocks that were interpreted as either a record of fracturing-healing cycles (Angiboust et al., 2012; Giuntoli et al., 2018; Broadwell et al., 2019) or element exchange along sub-grain boundaries (Konrad-Schmolke et al., 2007). The remarkable textural coupling between microchannels and the misorientated garnet domains (i.e., low-angle boundaries ± hairline fractures) in the studied eclogites (**Figure 4**) is compatible with fluid percolation along pre-existing low-angle boundaries, which acted as fluid pathways in the garnet grain interiors. The correlation of microchannels to hairline fractures (**Figures 4A,F**) is consistent with local microfracturing of garnet in the presence of overpressurized fluids. The lack of evidence for fluid-assisted deformation mechanisms, as well as the absence of heterogeneously distributed, interconnected reaction products in the undeformed rock volume that may represent fossilized fluid pathways at the rock scale (e.g., Macente et al., 2017 and references therein), suggest that fluids migrating along low-angle boundaries (±hairline fractures) were expelled from garnet grain interiors. Considering that the Mg-enriched microchannels cut the overall prograde core-to-rim Mg enrichment of garnet (**Figures 3B,C** vs. **Figures 3M,N**), the localized chemical heterogeneities along the low-angle boundaries (±hairline fractures) record fluid percolation close to the peak P–T conditions. The breakdown of lawsonite and likely glaucophane inclusions—a strong indication for fluid production during eclogitization–thus had significant implications for brittle failure of the rock, because the production of fluids was likely a key component for microfracturing of garnet grains along the amalgamation planes (**Figures 3**, **9**).

The lack of offset along these fractures through the amalgamated garnet clusters indicates an insignificant shear-stress component during fracturing. Thus, these fractures may be interpreted as hydrofractures that are a result of increased pore-fluid pressure due to lawsonite and glaucophane dehydration. Furthermore, the mineral assemblage identified within microfracture (**Figure 3**) provides conventional geothermobarometry estimates of ~2.47 GPa at ~620°C obtained for sample TS1758D, confirming that the microfractures were sealed at HP conditions. However, other mechanisms for fracturing can be considered. For example, expansion and fracturing of garnet due to volume reduction of matrix minerals, e.g., crystallization of eclogite facies omphacite from blueschist facies minerals (Engvik et al., 2001), thermal shock associated with intermediate-depth earthquakes as previously recognized in the rocks adjacent to

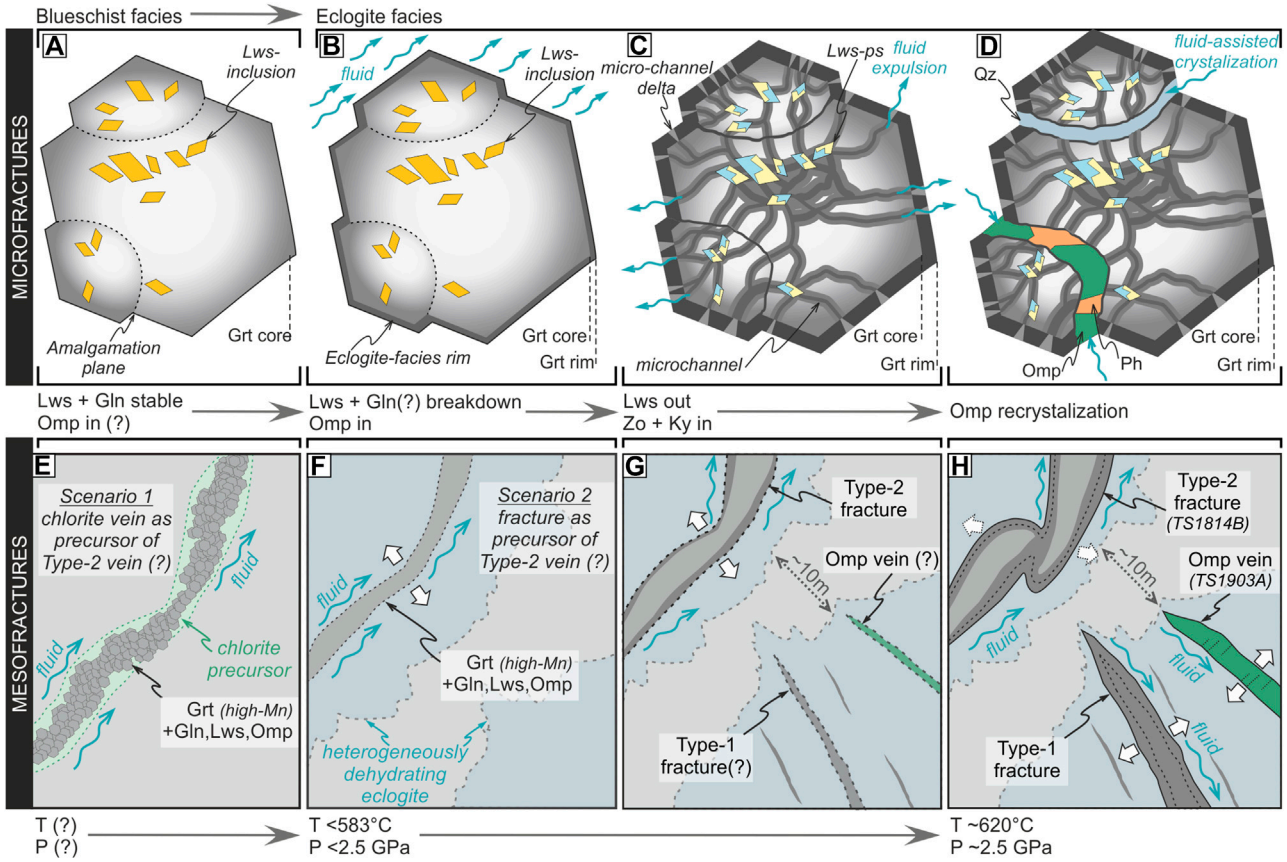

FIGURE 9 | A schematic model showing garnet growth and brittle deformation during eclogitization. **(A)** Amalgamation of garnet cores with abundant lawsonite inclusions at blueschist facies conditions. **(B)** Growth of garnet rim at incipient stages of eclogitization. **(C)** Microchannel development in garnet related with lawsonite- and glaucophane(?)-breakdown reactions. The released fluids formed vermicular microchannels and microchannel deltas propagating outwards towards the grain boundaries. **(D)** Further microscale fracturing, related with pore-fluid overpressure, and subsequent crystallization of high-pressure minerals in the newly formed fractures. **(E)** Scenario no.1 for initial formation of the Type-2, garnet-sealed mesofractures: crystallization of HP minerals (perhaps overprinting chlorite) in a pre-existing fracture due to pillow basalt quenching on the seafloor. **(F)** Scenario no.2 for formation of the Type-2 measofractures: initiation by fracturing at HP conditions. **(G)** A further dehydration and opening of Type-2 fracture, and the possible opening of the Type-1 fractures and Omp-sealed fractures, in the presence of fluid at HP conditions. **(H)** Final stage of vein formation. Type-2 vein is disrupted in the higher differential stress domain, whereas the Type-1 fracture and Omp-sealed fracture are fully developed in the higher pore-fluid pressure/lower effective stress domain. The distance of ~10 m on image G and H represent the spatial position of observed eclogites domains displaying rheological heterogeneity. Note that the illustrations are not to scale. Mineral abbreviations: Grt, garnet; Omp, omphacite; Lws, lawsonite; Gln, glaucophane; Zo, zoisite; Qz, quartz; Lws-ps, lawsonite pseudomorph; Ph, phengite.

pseudotachylytes (Papa et al., 2018), or decompression fractures within eclogite facies conditions (Straume and Austrheim, 1999). Volume reduction of the matrix minerals is a plausible mechanism to aid fracturing of the garnets, since the fractures are infilled by omphacite, phengite and quartz, representing expansion of the garnet clusters. However, thermal shock and decompression fracturing are not considered to be likely explanations. The fractured garnets are not observed to be spatially associated with pseudotachylytes (Papa et al., 2018), and decompression fractures have either been interpreted to be associated with volume increase during amphibolitization of eclogites (Straume and Austrheim, 1999) which did not occur in these samples. Therefore, the likely mechanisms for garnet fracturing are pore-fluid pressure increase due to lawsonite and glaucophane dehydration and volume decrease of the matrix during eclogitization.

The Type-1 and Type-2 mesofractures in eclogite bodies likely acted as fluid migration pathways in the subducting slab (Davies, 1999; Plümper et al., 2017a,b; Jamtveit et al., 2018), which strongly resemble HP fracture networks identified in the eclogitized blueschists of New Caledonia (Taetz et al., 2016, 2018). The Type-1 mesofractures strongly resemble the mode-I fractures (e.g., Pollard and Segall. 1987). In contrast, the dilational component and angular geometries of Type-2 mesofractures make interpretation more ambiguous as they may represent a mode-I fracture network or mixed-mode fracturing. The close spatial association of the two different mesofractures (<10 m apart) with different geometries suggests that stress was heterogeneous on the mesoscale. Such heterogeneities could arise from heterogeneous sea-floor hydration of the basalts and gabbros along permeable zones (e.g., fractures) prior to subduction (Peacock, 1993). This would cause variations in

mineral-bound H_2O within the rocks on the decameter scale during prograde metamorphism. As a result, the magnitude of dehydration reactions during eclogitization would be heterogeneous across the rock volume, producing variations in volume reduction, pore-fluid pressure and differential stress (Austrheim and Boundy, 1994; Comte and Suárez, 1994; Engvik et al., 2001; Lund and Austrheim, 2003; Ferrand, 2019). Likewise, it is plausible that the Type-2 mesofractures may also represent sea-floor processes as fractures that originally developed during quenching of pillow basalts on the ocean floor. In such a scenario, that the breccias would be inherited from the pillow basalt textures and the mesofractures would have been filled by mineral products of ocean-floor metamorphism such as chlorite (among others) that could have later been preferentially replaced by garnet and other HP phases. However, the presence of distinct vein-sealing zones with HP assemblages (the inner and outer zones) and the high-strain disrupted zone, also with a HP mineral assemblage, clearly demonstrates at least one episode of vein dilation at HP conditions. The conditions for sealing of the disrupted zone of ~2.42 GPa at ~635°C from conventional geothermobarometry, and ~620°C from trace element thermometry, provide robust evidence for the sealing under HP conditions during prograde to (near-)peak metamorphism (**Figures 8** and **9**). Furthermore, the Type-1 mesofractures do not reflect structures formed during quenching of pillow basalts and can be postulated to be primary HP fractures. Hence, whether the garnet veins originated from previous, chlorite-sealed fractures or if they initially formed during an eclogite facies brittle failure, the fluids that facilitated garnet growth operated under HP conditions (**Figure 9**).

The P–T conditions for microfracture development directly overlap the P-T conditions of mesofracture development, indicating that fracturing on both scales is intimately linked. This overall well-preserved fracture network in the Tsäkkok eclogites provides significant insight into the variations of pore-fluid pressure, volume changes, and possible variations of differential stress that are intimately related to fluid production and expulsion (**Figure 9**). Strong correlations between the hydrated portions of the slab where fluids are expulsed and locations of deep seismic events have been well-documented (e.g., Davies, 1999; Peacock, 2001; Hacker et al., 2003; Jung et al., 2004; Peacock, 2009; Fagereng and Diener, 2011; Hayman and Lavier, 2014; Audet and Kim, 2016; Wang et al., 2017). This relationship strongly suggests that dehydration-driven HP brittle deformation that is recorded in the Tsäkkok Lens may represent deep seismicity in a cold subducting slab. However, diagnostic features for seismicity, mainly pseudotachylytes or shear planes, remain equivocal within the Tsäkkok Lens eclogites, preventing unambiguous interpretation that brittle deformation in the Tsäkkok eclogites is in fact associated with deep seismicity. Nevertheless, the Tsäkkok Lens offers unique potential for future studies to understand fluid circulation in ancient subduction zones, and its possible seismic links.

CONCLUSION

The early Paleozoic Tsäkkok Lens eclogites constitute the oldest documented natural example of HP brittle deformation due to dehydration of lawsonite and glaucophane during eclogitization of blueschists. These metamorphic dehydration reactions were responsible for producing fluids that facilitated brittle fracturing of the eclogites under HP conditions due to increased pore-fluid pressure on the microscale. Brittle deformation may have also been promoted due to volume changes during eclogitization. These features are potentially linked with seismic events in a cold subduction regime.

DATA AVAILABILITY STATEMENT

The original contributions presented in the study are included in the article/**Supplementary Material**, further inquiries can be directed to the corresponding authors.

AUTHOR CONTRIBUTIONS

MB initiated the project and prepared figures. CB interpreted the structural data. MB and CB developed the main ideas and JM, PJ, SM, and BA also contributed. MB, CB, JM, PJ, SM, BA, KH, and IK contributed to writing the manuscript. MB, JM and KK interpreted the petrological data. MB, CB, PJ, IK, and JM participated in the fieldwork. MB, IK, and KK participated in EMP data acquisition. MB and JŠ participated in μ-CT data acquisition and interpretation. MB and KH participated in EBSD data acquisition and interpretation.

FUNDING

This research was funded by the National Science Centre (Poland) Project No. 2014/14/E/ST10/00321 (JM) and No. 2019/33/N/ST10/01479 (MB), as well as the Polish National Agency for Academic Exchange scholarship no. PPN/IWA/2018/1/00046/U/0001 (MB) and no. PPN/IWA/2018/1/00030/U/00001 (CB).

ACKNOWLEDGMENTS

We thank G. Ziemniak and C. J. Garrido for discussions; L. Tual for valuable help during the fieldwork; A. Włodek for technical and analytical assistance during WDS analyses at the AGH-UST. We are grateful for constructive reviews performed by L. Menegon and S. Ferrando leading to significant improvement of the manuscript, as well as T. P. Ferrand and anonymous reviewers who provided reviews on the earlier version of the manuscript. We also thank B.Grasemann for editorial handling of the manuscript.

SUPPLEMENTARY MATERIAL

The Supplementary Material for this article can be found online at: https://www.frontiersin.org/articles/10.3389/feart.2020.594453/full#supplementary-material.

REFERENCES

Ando, J., Fujino, K., and Takeshita, T. (1993). Dislocation microstructures in naturally deformed silicate garnets. *Phys. Earth Planet. In.* 80, 105–116. doi:10.1016/0031-9201(93)90041-7

Angiboust, S., and Agard, P. (2010). Initial water budget: The key to detaching large volumes of eclogitized oceanic crust along the subduction channel?. *Lithos* 120, 453–474. doi:10.1016/j.lithos.2010.09.007

Angiboust, S., Agard, P., Yamato, P., and Raimbourg, H. (2012). Eclogite breccias in a subducted ophiolite: a record of intermediate-depth earthquakes? *Geology* 40, 707–710. doi:10.1130/G32925.1

Angiboust, S., Yamato, P., Hertgen, S., Hyppolito, T., Bebout, G. E., and Morales, L. (2017). Fluid pathways and high pressure metasomatism in a subducted continental slice (Mt. Emilius klippe, W. Alps). *J. Metamorph. Geol.* 35, 471–492. doi:10.1111/jmg.12241

Audet, P., and Kim, Y. H. (2016). Teleseismic constraints on the geological environment of deep episodic slow earthquakes in subduction zone forearcs: a review. *Tectonophysics* 670, 1–15. doi:10.1016/j.tecto.2016.01.005

Austrheim, H., and Andersen, T. B. (2004). Pseudotachylytes from Corsica: fossil earthquakes from a subduction complex. *Terra Nov.* 16, 193–197. doi:10.1111/j.1365-3121.2004.00551.x

Austrheim, H., and Boundy, T. M. (1994). Pseudotachylytes generated during seismic faulting and eclogitization of the deep crust. *Science* 265, 82–83. doi:10.1126/science.265.5168.82

Bachmann, F., Hielscher, R., and Schaeben, H. (2010). Texture analysis with MTEX—Free and open source software Toolbox. *Solid State Phenom.* 160, 63–68. doi:10.4028/www.scientific.net/ssp.160.63

Ballèvre, M., Pitra, P., and Bohn, M. (2003). Lawsonite growth in the epidote blueschists from the Ile de Groix (Armorican Massif, France): a potential geobarometer. *J. Metamorph. Geol.* 21, 723–735. doi:10.1046/j.1525-1314.2003.00474.x

Barnes, C. J., Jeanneret, P., Kullerud, K., Majka, J., Schneider, D. A., Bukała, M., et al (2020). Exhumation of the high-pressure Tsäkkok lens, Swedish Caledonides: insights from the structural and white mica 40 Ar/39 Ar geochronological record. *Tectonics* 39, 1–13. doi:10.1029/2020TC006242

Bearth, P. (1973). Gesteins- und Mineralparagenesen aus den Ophiolithen von Zermatt. *Schweiz. Mineral. Petro. Mitt.* 53, 299–334.

Behr, W. M., Kotowski, A. J., and Ashley, K. T. (2018). Dehydration-induced rheological heterogeneity and the deep tremor source in warm subduction zones. *Geology* 46, 475–478. doi:10.1130/G40105.1

Broadwell, K. S., Locatelli, M., Verlaguet, A., Agard, P., and Caddick, M. J. (2019). Transient and periodic brittle deformation of eclogites during intermediate-depth subduction. *Earth Planet Sci. Lett.* 521, 91–102. doi:10.1016/j.epsl.2019.06.008

Brudzinski, M., Clifford, H. T., Hacker, B. R., and Engdahl, E. R. (2007). Global prevalence of double benioff zones. *Science* 316, 1472–1474. doi:10.1126/science.1139204

Comte, D., and Suárez, G. (1994). An inverted double seismic zone in Chile: evidence of phase transformation in the subducted slab. *Science* 263, 212–215. doi:10.1126/science.263.5144.212

Crawford, W. A., and Fyfe, W. S. (1965). Lawsonite equilibria. *Am. J. Sci.* 263, 262–270. doi:10.2475/ajs.263.3.262

Davies, J. H. (1999). The role of hydraulic fractures and intermediate-depth earthquakes in generating subduction-zone magmatism. *Nature* 398, 142–145. doi:10.1038/18202

Deseta, N., Andersen, T. B., and Ashwal, L. D. (2014). A weakening mechanism for intermediate-depth seismicity? detailed petrographic and microtextural observations from blueschist facies pseudotachylytes, Cape Corse, Corsica. *Tectonophysics* 610, 138–149. doi:10.1016/j.tecto.2013.11.007

Engvik, A. K., Austrheim, H., and Erambert, M. (2001). Interaction between fluid flow, fracturing and mineral growth during eclogitization, an example from the Sunnfjord area, Western Gneiss Region, Norway. *Lithos* 57, 111–141. doi:10.1016/s0024-4937(01)00037-8

Fagereng, Å., and Diener, J. F. A. (2011). Non-volcanic tremor and discontinuous slab dehydration. *Geophys. Res. Lett.* 38, 1–5. doi:10.1029/2011GL048214

Ferrand, T. P., Hilairet, N., Incel, S., Deldicque, D., Labrousse, L., Gasc, J., et al (2017). Dehydration-driven stress transfer triggers intermediate-depth earthquakes. *Nat. Commun.* 8, 1–11. doi:10.1038/ncomms15247

Ferrand, T. P. (2019). Seismicity and mineral destabilizations in the subducting mantle up to 6 GPa, 200 km depth. *Lithos* 334-335, 205–230. doi:10.1016/j.lithos.2019.03.014

Florez, M. A., and Prieto, G. A. (2019). Controlling factors of seismicity and geometry in double seismic zones. *Geophys. Res. Lett.* 46, 4174–4181. doi:10.1029/2018gl081168

Fry, N., and Fyfe, W. S. (1969). Eclogites and water pressure. *Contrib. Miner. Petrol.* 24, 1–6. doi:10.1007/bf00398749

Fry, N. (1973). Lawsonite pseudomorphed in Tauern greenschist. *Miner. Mag.* 39, 121–122. doi:10.1180/minmag.1973.039.301.21

Ganguly, J., Cheng, W., and Tirone, M. (1996). Thermodynamics of aluminosilicate garnet solid solution: new experimental data, an optimized model, and thermometric applications. *Contrib. Miner. Petrol.* 126, 137–151. doi:10.1007/s004100050240

Gao, J., and Klemd, R. (2001). Primary fluids entrapped at blueschist to eclogite transition: evidence from the Tianshan meta-subduction complex in northwestern China. *Contrib. Miner. Petrol.* 142, 1–14. doi:10.1007/s004100100275

García-Casco, A., Torres-Roldán, R. L., Millán, G., Monié, P., and Schneider, J. (2002). Oscillatory zoning in eclogitic garnet and amphibole, Northern Serpentinite Melange, Cuba: a record of tectonic instability during subduction? *J. Metamorph. Geol.* 20, 581–598. doi:10.1046/j.1525-1314.2002.00390.x

Giuntoli, F., Lanari, P., and Engi, M. (2018). Deeply subducted continental fragments—Part 1: fracturing, dissolution–precipitation, and diffusion processes recorded by garnet textures of the central Sesia Zone (western Italian Alps). *Solid Earth* 9, 167–189. doi:10.5194/se-9-167-2018

Hacker, B. R., Peacock, S. M., Abers, G. A., and Holloway, S. D. (2003). Subduction factory 2. Are intermediate-depth earthquakes in subducting slabs linked to metamorphic dehydration reactions?. *J. Geophys. Res.* 108, 1–16. doi:10.1029/2001JB001129

Hasegawa, A., Umino, N., and Takagi, A. (1978). Double-planed structure of the deep seismic zone in the northeastern Japan arc. *Tectonophysics* 47, 43–58. doi:10.1016/0040-1951(78)90150-6

Hawemann, F., Mancktelow, N., Wex, S., Pennacchioni, G., and Camacho, A. (2019). Fracturing and crystal plastic behaviour of garnet under seismic stress in the dry lower continental crust (Musgrave Ranges, Central Australia). *Solid Earth* 10, 1635–1649. doi:10.5194/se-10-1635-2019

Hayman, N. W., and Lavier, L. L. (2014). The geologic record of deep episodic tremor and slip. *Geology* 42, 195–198. doi:10.1130/G34990.1

Heinrich, W., and Althaus, E. (1988). Experimental determination of the reactions 4 lawsonite + 1 albite <=> 1 paragonite + 2 zoisite + 2 quartz + 6 H_2O and 4 lawsonite + 1 jadeite <=> 1 paragonite + 2 zoisite + 1 quartz + 6 H_2O. *Neues Jahrbuch Miner. Abhand.* 11, 516–528.

Hielscher, R., and Schaeben, H. (2008). A novel pole figure inversion method: specification of the MTEX algorithm. *J. Appl. Cryst.* 41, 1024–1037. doi:10.1107/s0021889808030112

Holland, T. J. B. (1990). Activities in omphacite solid solutions: an application of Landau theory to mixtures. *Contrib. Miner. Petrol.* 105, 446–453. doi:10.1007/bf00286831

Holland, T. J. B., and Powell, R. (1998). An internally consistent thermodynamic data set for phases of petrological interest. *J. Metamorph. Geol.* 16, 309–343. doi:10.1111/j.1525-1314.1998.00140.x

Incel, S., Hilairet, N., Labrousse, L., John, T., Deldicque, D., Ferrand, T., et al (2017). Laboratory earthquakes triggered during eclogitization of lawsonite-bearing blueschist. *Earth Planet Sci. Lett.* 459, 320–331. doi:10.1016/j.epsl.2016.11.047

Ingrin, J., and Madon, M. (1995). TEM observations of several spinel-garnet assemblies: toward the rheology of the transition zone. *Terra Nova* 7, 509–515. doi:10.1111/j.1365-3121.1995.tb00552.x

Jamtveit, B., Ben-Zion, Y., Renard, F., and Austrheim, H. (2018). Earthquake-induced transformation of the lower crust. *Nature* 556, 487–491. doi:10.1038/s41586-018-0045-y

John, T., and Schenk, V. (2006). Interrelations between intermediate-depth earthquakes and fluid flow within subducting oceanic plates: constraints from eclogite facies pseudotachylytes. *Geology* 34, 557–560. doi:10.1130/G22411.1

Jung, H., Green II, H. W., and Dobrzhinetskaya, L. F. (2004). Intermediate-depth earthquake faulting by dehydration embrittlement with negative volume change. *Nature* 428, 545–549. doi:10.1038/nature02412

Kita, S., and Ferrand, T. P. (2018). Physical mechanisms of oceanic mantle earthquakes: comparison of natural and experimental events. *Sci. Rep.* 8, 149–171. doi:10.1038/s41598-018-35290-x

Konrad-Schmolke, M., O'Brien, P. J., and Heidelbach, F. (2007). Compositional re-equilibration of garnet: the importance of sub-grain boundaries. *Eur. J. Mineral.* 19, 431–438. doi:10.1127/0935-1221/2007/0019-1749

Kullerud, K. (1987). *Origin and tectonometamorphic evolution of the eclogites in the Tsäkkok lens (Seve Nappes). Cand. Scient. thesis. [Oslo, Norway]*. Southern Norrbotten (Sweden): University of Oslo.

Kullerud, K., Stephens, M. B., and Zachrisson, E. (1990). Pillow lavas as protoliths for eclogites: evidence from a late Precambrian-Cambrian continental margin, Seve Nappes, Scandinavian Caledonides. *Contrib. Mineral. Petrol.* 105, 1–10. doi:10.1007/bf00320962

Lanari, P., Vidal, O., Andrade, V. De., Dubacq, B., Lewin, E., Grosch, E. G., et al (2014). XMapTools : a MATLAB © -based program for electron microprobe X-ray image processing and geothermobarometry. *Comput. Geosci.* 62, 227–240. doi:10.1016/j.cageo.2013.08.010

Liou, J. G. (1971). P–T stabilities of laumontite, wairakite, lawsonite, and related minerals in the system $CaAl_2Si_2O_8$–SiO_2–H_2O. *J. Petrol.* 12, 379–411. doi:10.1093/petrology/12.2.379

Lund, M. G., and Austrheim, H. (2003). High-pressure metamorphism and deep-crustal seismicity: evidence from contemporaneous formation of pseudotachylytes and eclogite facies coronas. *Tectonophysics* 372, 59–83. doi:10.1016/S0040-1951(03)00232-4

Macente, A., Fusseis, F., Menegon, L., Xiao, X., and John, T. (2017). The strain-dependent spatial evolution of garnet in a high-P ductile shear zone from the Western Gneiss Region (Norway): a synchrotron X-ray microtomography study. *J. Metamorph. Geol.* 35, 565–583. doi:10.1111/jmg.12245

Magott, R., Fabbri, O., and Fournier, M. (2016). Subduction zone intermediate-depth seismicity: insights from the structural analysis of Alpine high-pressure ophiolite-hosted pseudotachylyte (Corsica, France). *J. Struct. Geol.* 87, 95–114. doi:10.1016/j.jsg.2016.04.002

Mainprice, D., Bascou, J., Cordier, P., and Tommasi, A. (2004). Crystal preferred orientations of garnet: comparison between numerical simulations and electron back-scattered diffraction (EBSD) measurements in naturally deformed eclogites. *J. Struct. Geol.* 26, 2089–2102. doi:10.1016/j.jsg.2004.04.008

Mørk, M. B. E., Kullerud, K., and Stabel, A. (1988). Sm-Nd dating of Seve eclogites, norrbotten, Sweden - evidence for early Caledonian (505 Ma) subduction. *Contrib. Mineral. Petrol.* 99, 344–351. doi:10.1007/BF00375366

Newton, R. C., and Kennedy, G. C. (1963). Some equilibrium reactions in the join $CaAl_2Si_2O_8$–H_2O. *J. Geophys. Res.* 68, 2967–2983. doi:10.1029/jz068i010p02967

Obara, K. (2002). Nonvolcanic deep tremor associated with subduction in southwest Japan. *Science* 296, 1679–1681. doi:10.1126/science.1070378

Okazaki, K., and Hirth, G. (2016). Dehydration of lawsonite could directly trigger earthquakes in subducting oceanic crust. *Nature* 530, 81–84. doi:10.1038/nature16501

Orozbaev, R., Hirajima, T., Bakirov, A., Takasu, A., Maki, K., Yoshida, K., et al (2015). Trace element characteristics of clinozoisite pseudomorphs after lawsonite in talc-garnet-chloritoid schists from the Makbal UHP Complex, northern Kyrgyz Tian-Shan. *Lithos* 226, 98–115. doi:10.1016/j.lithos.2014.10.008

Palin, R. M., and White, R. W. (2016). Emergence of blueschists on Earth linked to secular changes in oceanic crust composition. *Nat. Geosci.* 9, 60–64. doi:10.1038/ngeo2605

Papa, S., Pennacchioni, G., Angel, R. J., and Faccenda, M. (2018). The fate of garnet during (deep-seated) coseismic frictional heating: The role of thermal shock. *Geology* 46, 471–474. doi:10.1130/g40077.1

Peacock, S. M. (1993). The importance of blueschist → eclogite dehydration reactions in subducting oceanic crust. *Geol. Soc. Am. Bull.* 105, 684–694. doi:10.1130/0016-7606(1993)105<0684:tiobed>2.3.co;2

Peacock, S. M. (2001). Are the lower planes of double seismic zones caused by serpentine dehydration in subducting oceanic mantle? *Geology* 29, 299–302. doi:10.1130/0091-7613(2001)029<0299:atlpod>2.0.co;2

Peacock, S. M. (2009). Thermal and metamorphic environment of subduction zone episodic tremor and slip. *J. Geophys. Res.* 114, 1–9. doi:10.1029/2008JB005978

Philippon, M., Gueydan, F., Pitra, P., and Brun, J.-P. (2013). Preservation of subduction-related prograde deformation in lawsonite pseudomorph-bearing rocks. *J. Meta. Geol.* 31, 571–583. doi:10.1111/jmg.12035

Plümper, O., John, T., Podladchikov, Y. Y., Vrijmoed, J. C., and Scambelluri, M. (2017a). Fluid escape from subduction zones controlled by channel-forming reactive porosity. *Nat. Geosci.* 10, 150–156. doi:10.1038/ngeo2865

Plümper, O., Botan, A., Los, C., Liu, Y., Malthe-Sørenssen, A., and Jamtveit, B. (2017b). Fluid-driven metamorphism of the continental crust governed by nanoscale fluid flow. *Nat. Geosci.* 10, 685–690. doi:10.1038/NGEO3009

Pollard, D., and Segall, P. (1987). 8-theoretical displacements and stresses near fractures in rock: with applications to faults, joints, veins, dikes, and solution surfaces. *Fracture mechanics of rock*. Editor B. K. Atkinson (London, UK: Academic Press), 277–349.

Pouchon, J-L., and Pichoir, F. (1988). A simplified version of the 'PAP' model for matrix corrections in EMPA in *Microbeam analysus*. Editor D.E. Newburry (San Francisco, CA, United States: San Francisco Press), 315–318.

Ravna, E. J. K. (2000). The garnet–clinopyroxene Fe^{2+}–Mg geothermometer: an updated calibration. *J. Metamorph. Geol.* 18, 211–219.

Ravna, E. J. K., Andersen, T. B., Jolivet, L., and De Capitani, C. (2010). Cold subduction and the formation of lawsonite eclogite—constraints from prograde evolution of eclogitized pillow lava from Corsica. *J. Metamorph. Geol.* 28, 381–395. doi:10.1111/j.1525-1314.2010.00870.x

Ravna, E. J. K., and Paquin, J. (2003). Thermobarometric methodologies applicable to eclogites and garnet ultrabasites. *EMU Notes Mineral.* 5, 229–259.

Ravna, E. J. K., and Terry, M. P. (2004). Geothermobarometry of UHP and HP eclogites and schists—an evaluation of equilibria among garnet–clinopyroxene–kyanite–phengite–coesite/quartz. *J. Metamorph. Geol.* 22, 579–592. doi:10.1111/j.1525-1314.2004.00534.x

Ren, Y., Chen, D., Kelsey, D. E., Gong, X., and Liu, L. (2017). Petrology and geochemistry of the lawsonite (pseudomorph)-bearing eclogite in Yuka terrane, North Qaidam UHPM belt: an eclogite facies metamorphosed oceanic slice. *Gondwana Res.* 42, 220–242. doi:10.1016/j.gr.2016.10.011

Rogers, G., and Dragert, H. (2003). Episodic tremor and slip on the Cascadia subduction zone: The chatter of silent slip. *Science* 300, 1942–1943. doi:10.1126/science.1084783

Root, D., and Corfu, F. (2012). U–Pb geochronology of two discrete Ordovician high-pressure metamorphic events in the Seve Nappe Complex, Scandinavian Caledonides. *Contrib. Miner. Petrol* 163, 769–788. doi:10.1007/s00410-011-0698-0

Scambelluri, M., Pennacchioni, G., Gilio, M., Bestmann, M., Plümper, O., and Nestola, F. (2017). Fossil intermediate-depth earthquakes in subducting slabs linked to differential stress release. *Nat. Geosci.* 10, 960–966. doi:10.1038/s41561-017-0010-7

Schmidt, M. W., and Poli, S. (1998). Experimentally based water budgets for dehydrating slabs and consequences for arc magma generation. *Earth Planet Sci. Lett.* 163, 361–379. doi:10.1016/s0012-821x(98)00142-3

Smit, M. A., and Pogge von Strandmann, P. A. E. (2020). Deep fluid release in warm subduction zones from a breached slab seal. *Earth Planet Sci. Lett.* 534, 116046. doi:10.1016/j.epsl.2019.116046

Smit, M. A., Scherer, E. E., John, T., and Janssen, A. (2011). Creep of garnet in eclogite: mechanisms and implications. *Earth Planet Sci. Lett.* 311, 411–419. doi:10.1016/j.epsl.2011.09.024

Storey, C. D., and Prior, D. J. (2005). Plastic deformation and recrystallization of garnet: a mechanism to facilitate diffusion creep. *J. Petrol.* 46, 2593–2613. doi:10.1093/petrology/egi067

Straume, A. K., and Austrheim, H. (1999). Importance of fracturing during retro-metamorphism of eclogites. *J. Metamorph. Geol.* 17, 637–652. doi:10.1046/j.1525-1314.1999.00218.x

Stünitz, H., Neufeld, K., Heilbronner, R., Finstad, A. K., Konopásek, J., and Mackenzie, J. R. (2020). Transformation weakening: diffusion creep in eclogites as a result of interaction of mineral reactions and deformation. *J. Struct. Geol.* 139, 104129. doi:10.1016/j.jsg.2020.104129

Taetz, S., John, T., Bröcker, M., and Spandler, C. (2016). Fluid-rock interaction and evolution of a high-pressure/low-temperature vein system in eclogite from New Caledonia: insights into intraslab fluid flow processes. *Contrib. Miner. Petrol.* 171, 1–27. doi:10.1007/s00410-016-1295-z

Taetz, S., John, T., Bröcker, M., Spandler, C., and Stracke, A. (2018). Fast intraslab fluid-flow events linked to pulses of high pore fluid pressure at the subducted plate interface. *Earth Planet Sci. Lett.* 482, 33–43. doi:10.1016/j.epsl.2017.10.044

Terry, M. P., and Heidelbach, F. (2004). Superplasticity in garnet from eclogite facies shear zones in the Haram Gabbro, Haramsøya, Norway. *Geology* 32, 281–284. doi:10.1130/g20157.1

Tomkins, H. S., Powell, R., and Ellis, D. J. (2007). The pressure dependence of the zirconium-in-rutile thermometer. *J. Metamorph. Geol.* 25, 703–713. doi:10.1111/j.1525-1314.2007.00724.x

Trepmann, C. A., and Stöckhert, B. (2002). Cataclastic deformation of garnet: a record of synseismic loading and postseismic creep. *J. Struct. Geol.* 24, 1845–1856. doi:10.1016/s0191-8141(02)00004-4

Viete, D. R., Hacker, B. R., Allen, M. B., Seward, G. G. E., Tobin, M. J., Kelley, C. S., et al (2018). Metamorphic records of multiple seismic cycles during subduction. *Sci. Adv.* 4, 1–14. doi:10.1126/sciadv.aaq0234

Voegelé, V., Liu, B., Cordier, P., Wang, Z., Takei, H., Pan, P., et al (1999). High temperature creep in a 2–3–4 garnet: $Ca_3Ge_2Ge_3O_{12}$. *J. Mater. Sci.* 34, 4783–4791. doi:10.1023/a:1004695307022

Wang, S. J., Wang, L., Brown, M., Piccoli, P. M., Johnson, T. E., Feng, P., et al (2017). Fluid generation and evolution during exhumation of deeply subducted UHP continental crust: petrogenesis of composite granite-quartz veins in the Sulu belt, China. *J. Metamorph. Geol.* 35, 601–629. doi:10.1111/jmg.12248

Wang, Z., and Ji, S. (1999). Deformation of silicate garnets: brittle ductile transition and its geological implications. *Can. Miner.* 37, 525–541.

Whitney, D. L. (1996). Garnets as open systems during regional metamorphism. *Geology* 24, 147–150. doi:10.1130/0091-7613(1996)024<014710.1130/0091-7613(1996)024<0147:gaosdr>2.3.co;2

Xu, L., Mei, S., Dixon, N., Jin, Z., Suzuki, A. M., and Kohlstedt, D. L. (2013). Effect of water on rheological properties of garnet at high temperatures and pressures. *Earth Planet Sci. Lett.* 379, 158–165. doi:10.1016/j.epsl.2013.08.002

Conflict of Interest: The authors declare that the research was conducted in the absence of any commercial or financial relationships that could be construed as a potential conflict of interest.

The handling editor declared a past co-authorship with one of the authors, BA.